J. Phys. Chem. A **2001,** *105,* 3340−3358

The Geometric and Electronic Structures of Niobium Carbon Clusters

Hugh Harris and Ian Dance*

School of Chemistry, University of New South Wales, Sydney, NSW 2052, Australia

Received: September 28, 2000; In Final Form: January 10, 2001

More than 50 $[Nb_xC_y]^+$ clusters have been observed in the gas phase. We report a density functional investigation of 100 isomers of 28 of the most prominent of these clusters, ranging in size from $[Nb_2C_2]$ to $[Nb_{12}C_{20}]$ and $[Nb_{14}C_{16}]$, calculated as both neutral and monocation species. Vertical ionization energies and normalized binding energies are provided for all isomers, and the most probable structures of the 28 $[Nb_xC_y]$ clusters are assigned. The species $[Nb_8C_{12}]$ and $[Nb_{14}C_{13}]$ have the same structures (T_d and O_h, respectively) as the Ti analogues. The calculations and interpretations generate a broad picture of the geometric structures, electronic structures, and observed reactivities of Nb_xC_y clusters. The relevant structural principles and the key substructural components have been defined. At the local level, Nb−C bonding is the principal source of stability, together with C−C bonding where it occurs, whereas Nb−Nb bonding energy is less important but still significant. Cradle-motif Nb_4C_2 moieties are important, but not if they are strongly distorted. The 3-fold wheel substructure and the spire (3-fold or 4-fold) are key substructures involving C_2. Fused cubanoid units as occur in the nanocrystallites are the main containers of isolated C atoms and are usually slightly distorted. Substitution of C_2 in place of C in a nanocrystallite occurs in some Nb_xC_y clusters that are slightly C-rich. Fusion of wheels or spires onto nanocrystallite sections occurs with increasing C content, and the most C-rich clusters contain C_2 units only, but not longer C_n chains.

Introduction

In the past decade, a variety of types and instances of metal carbon binary molecules have been uncovered experimentally, including (1) endohedral, exohedral, and networked metallofullerenes MC_n,[1−8] (2) graphitic MC_n,[1] (3) metallocarbohedrenes M_xC_y with C_2 groups, and nanodimensional fragments of MC lattices containing C atoms.[9−47] These unprecedented and unpredictable systems raise many fundamental questions and intimate opportunities for further science and technology. All of this experimental work has involved the molecules or ions in the gas phase, and the principal experimental information on them involves their stabilities to dissociation[15,17,24,25,36,40] and their reactions with a range of molecules including oxygen, water, acetonitrile, ammonia, benzene, alkyl halides, alcohols, and acetone.[20−22,28,33,36,43−48] Bowers et al. have determined their collisional cross-sections, measured as drift times through inert gas.[49−51] Wang, Li, and Wu have applied a photoelectron spectroscopy technique to measure electron affinities of a range of species.[39,42] Meijer, Duncan, and co-workers have recently reported IR data for several M_xC_y species.[52,53]

Following the first report of Ti_8C_{12} in 1992,[11] most attention has concentrated on the metallocarbohedrene $M_8(C_2)_6$ and on the nanocrystallite class of clusters M_xC_y in which $y/x \approx 1$. The metallocarbohedrenes are regarded as polyhedral frameworks of M atoms and C_2 groups (in some cases with C_n higher than C_2).[11,32,54−57] Alternatively, the gas-phase nanocrystallites can be regarded as fragments of the face-centered cubic lattice adopted by the nonmolecular solid MC compounds and, thus, are conceived of only in terms of C atoms bonded to M.[32,57] The differentiation of M_xC_y clusters as metallocarbohedrenes or nanocrystallites is based largely on the stable compositions observed mass spectrometrically and on their dissociation behavior. However, this is an oversimplification, because it is likely that many clusters contain both isolated C atoms and C−C bonded groups. In this context, the photoextrusions of metal atoms from M_xC_y are significant, as they must at some stage involve C−C bond formation, as in the sequence of photoextrusions from $[Ti_{14}C_{13}]^+$ to $[Ti_8C_{13}]^+$.[25,58]

Early first transition series metals such as titanium show a superabundance of $[M_8C_{12}]^+$ and a lesser amount of $[M_{14}C_{13}]^+$. Tantalum shows only compositions with $y/x \approx 1$,[59,60] whereas Nb[26,30] and Fe[25] have complicated abundance distributions that are highly sensitive to formation conditions. One of the key questions in this research is the influence of the electronic properties of the metal in the formation and stabilization of the various types of M_xC_y clusters.

In this paper we report theoretical investigations of the niobium clusters $[Nb_xC_y]$, which have been the subject of four complementary experimental investigations. The $[Nb_xC_y]$ clusters are generated in pulsed laser vaporization sources, in which Nb clustering occurs in the presence of hydrocarbons, which are dehydrogenated. Castleman et al.[26] showed that variations in the formation conditions lead to different distributions of products and concluded that the two main structure types, met−car and nanocrystallite, form in parallel and are kinetically controlled. Their metastable decay results also provide insights into the stability of observed species. Pilgrim, Brock and Duncan[30] also found sensitivity to growth conditions, and with better resolution of the manifolds of products and photofragmentation spectra, provided a more detailed picture of the compositions and stabilities. Freiser, Hay, et al. focused on $[Nb_4C_2]$, $[Nb_4C_4]$, and $[Nb_6C_7]$, reporting collisionally induced dissociation; reactions with dioxygen, water, and methanol; and calculated electronic and geometric structures.[22,47]

Figure 1 is a map of the compositions and relative abundances

---

* Author to whom correspondence should be addressed. E-mail: I.Dance@unsw.edu.au.

10.1021/jp0035535 CCC: $20.00

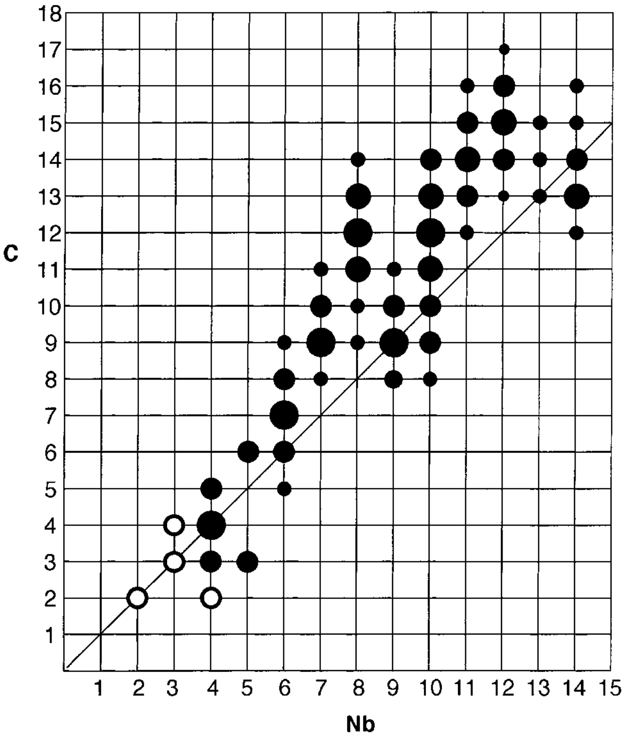

Figure 1. Map of commonly observed compositions of binary $[Nb_xC_y]^+$ clusters produced by laser ablation of Nb metal and cooling/clustering in hydrocarbons. Relative dot size indicates observed abundance. The diagonal line emphasizes the 1:1 Nb/C ratio. Compositions represented with an open circle are observed only through photodissociation.

of the more prominent $[Nb_xC_y]^+$ clusters that have been commonly observed in the various experiments.[22,26,30,47] Only well-resolved species from the cited sources are included in this figure; other compositions that are not shown might occur. The abundances presented in Figure 1 are based on results given by Duncan,[30] but as noted, the observed product distributions are sensitive to formation conditions. Prominent species in the product distributions for $[Nb_xC_y]^+$ are x/y = 4/4, 6/7, 7/9, 9/9, 10/12, 11/14, and 12/15. These compositions are not prominent for other metals such as Ti, V, or Fe. Unlike other metal−carbon systems that photodissociate M or MC_n from larger clusters,[15] Nb is observed to photodissociate C atoms. A significant conclusion is that niobium−carbon clusters are different from those of other early transition metals.[30]

The observed niobium−carbon clusters and their diversity raise the following questions. What are their probable geometric structures, and what are the important structural principles for $[Nb_xC_y]$ clusters? What are the electronic structures and general bonding principles of these species? Can this information be used to explain the observed distribution and reactivity of ions? Which properties, such as ionization potential or thermodynamic stability, are responsible for the observation of particular species? The concluding statement of the paper by Duncan and co-workers[30] states "Ab initio calculations would be especially valuable to test the stabilities and structures for these particular clusters and to explain why niobium−carbon clusters in general are so different from other transition metal systems."

Density functional theory (DFT) is especially suited to evaluation of the questions raised by these experiments. Because DFT is expedient for large inorganic clusters, and clusters with large atoms,[61−74] it can deal with the very large number of isomers that are possible for the many compositions. The geometry−energy surfaces for the $[Nb_xC_y]$ clusters can be explored, and the comparative energies for different compositions evaluated, with accuracy sufficient to provide a broad understanding for metal−carbon clusters.

The objective of this paper is to describe the structures, properties, and structural principles for the $[Nb_xC_y]$ clusters. We have selected 28 significant compositions from $[Nb_2C_2]$ to $[Nb_{14}C_{16}]$, and for them, we have made calculations for 100 postulated isomers. We present postulated and optimized structures for these isomers, compare their energies, extract pertinent geometrical principles, and describe characteristic features of electronic structure. Our goal is to generate the overall picture, prior to the examination of specific detail.

Methodology

The general investigative strategy involved postulation of possible structures for each composition, optimization of those structures by energy minimization, and recognition of resulting features that appeared to confer stability, followed by further postulation of structures incorporating those structural principles. The strategy and methodology are the same as used previously for MnS clusters.[75]

The postulation of structures for the $[Nb_xC_y]$ clusters was based on knowledge of (1) geometrical isomerism for other carbohedrenes of the early transition metals, particularly for compositions M_8C_{12}, M_8C_{13}, and $M_{14}C_{13}$; (2) the structures of intermediates M_xC_{13}, $x = 13-9$, in the sequential photodissociation of $Ti_{14}C_{13}$ to Ti_8C_{13};[58] and (3) the regular fragments of the cubic MC lattice, as suggested by Duncan.[24] In addition, we use the similarities between the structures of clusters M_xE_y for E = S, O and E = C_2.[76]

Density functional calculations used the program DMol, versions 2.36 and 960.[71,77,78] The density functionals used are the Lee−Yang−Parr functional for correlation[79] and Becke for exchange,[80] including nonlocal corrections that were applied post-SCF. Double numerical basis sets[71] included polarization functions for metals and carbon. Calculations were spin-restricted, and core orbitals were frozen. The electronic states of the molecules were not specified in the initial calculations; by use of smearing of electron population close to the Fermi level, the optimization was allowed access to low-lying electronic states. This is desirable in the initial investigation of the gross features of the geometry−energy surfaces, where various electronic states could be involved, and the objective is to locate the most stable structures. Subsequent energy minimization for each principal geometrical isomer focused on the electronic ground state by reducing any population smearing to zero or near zero. Energy surfaces for specific ground or excited electronic states have not been explicitly evaluated. Structures with small HOMO−LUMO gaps (<0.2 eV) and energetically close electronic states are identified in Table 1.

Postulated structures were initially optimized in the highest possible Abelian symmetry. For each structure, once the overall geometry was optimized in this symmetry, the structure was evaluated further by optimization after distortion and reduction of symmetry. This provided insight into the quality of the stationary point on the energy hypersurface (saddle point or minimum) and the steepness of the gradients. Some stationary points were assessed also on the basis of second derivative calculations, evaluated as the vibrational frequencies (available as Supporting Information). The energies presented and tabulated do not include zero-point or thermal corrections.

Details of the optimized structures are presented in Table 1. The point group symmetries used in the least constrained and final phases of structure optimzation are listed, together with the highest possible symmetry of the isomer. Quoted ionization

TABLE 1: Calculated Properties of [Nb$_x$C$_y$] Clusters[a]

					binding energies (kcal mol^{-1})					HOMO−LUMO gap (eV)	
	symmetry			distribution of C atom types	neutral		cation				
isomer	const[b]	actual[c]	ideal[d]		BE(0)[e]	ΔBE(0)[e]	BE(+)[e]	ΔBE(+)[e]	IE (eV)	neutral	cation
2/2A	C_1	D_{2h}	D_{2h}	$(\mu\text{-C})_2$	−428	0	−284	0	6.33	0.54	1.65
2/2B	C_1	C_s	C_s	$(\mu\text{-C}_2)$	−420	8	−265	19	6.89	0.60	0.51
2/2C	C_1	$D_{\infty h}$	$D_{\infty h}$	$(\mathrm{C}_{\mathrm{terminal}})_2$	−278	150	−134	150	7.20	0.21	0.73
3/3A	C_1	C_s	C_s	$(\mu_3\text{-C})(\mu\text{-C})_2$	−693	0	−566	0	5.59	0.37	1.15
3/3B	C_2	C_2	C_{2v}	$(\mu_3\text{-C})_2(\mu\text{-C})$	−679	14	−549	17	5.81	0.72	0.68
3/3C	C_1	C_1	C_1	$(\mu_3\text{-C})(\mu\text{-C}_2)$	−672	21	−535	31	6.11	0.34	0.45
3/3D	C_s	C_{3v}	C_{3v}	$(\mu\text{-C})_3$	−652	41	−528	38	5.64	0.25	1.15
3/3E	C_s	C_{2v}	C_{2v}	$(\mu\text{-C})_2(\mu_3\text{-C})$	−657	36	−523	43	5.72	0.07	0.31
3/3F	C_s	D_{3h}	D_{3h}	$(\mu\text{-C})_3$	−595	98	−454	112	6.16	0.04	0.13
3/4A	C_{3v}	C_{3v}	C_{3v}	$(\mu\text{-C})_3(\mu_3\text{-C})$	−844	0	−686	0	6.85	1.81	2.14
4/2A	C_2	C_{2v}	C_{2v}	$(\mu_3\text{-C})_2$	−650	0	−523	0	5.59	0.66	2.27
4/2B	C_2	C_{2v}	C_{2v}	$(\mu\text{-C})_2$	4/2A[f]		4/2A[f]		6.03	1.27	0.92
4/3A	C_{3v}	C_{3v}	C_{3v}	$(\mu_3\text{-C})_3$	−844	0	−715	0	5.77	1.15	1.40
4/4A	C_1	D_{2d}	T_d	$(\mu_3\text{-C})_4$	−1008	0	−901	0	5.12	0.27	0.31
4/4B	C_1	D_{2h}	D_{2h}	$(\mu_4\text{-C}_2)_2$	−962	46	−839	62	5.33	0.36	0.54
4/4C	C_1	C_s	C_s	$(\mu\text{-C})_3(\mu_4\text{-C})$	−948	60	−804	97	6.37	0.92	0.97
4/4D	C_1	D_{2d}	D_{2d}	$(\mu_4\text{-C}_2)_2$	−940	68	−804	97	6.29	1.04	0.87
4/4E	C_1	C_1	C_2	$(\mu\text{-C}_2)_2$	−919	89	−786	115	6.29	0.52	0.26
4/4F	C_1	C_1	C_2	$(\mu\text{-C}_2)_2$	−902	106	−777	124	6.29	0.55	0.28
4/4G	D_{2h}	D_{2h}	D_{2h}	$(\mu\text{-C})_4$	−866	142	−737	164	5.64	0.39	0.24
4/4H	C_{2h}	C_{2h}	C_{2h}	$(\mu\text{-C}_4)$	−858	150	−727	174	5.72	0.21	0.12
5/3A	C_s	C_s	C_{3v}	$(\mu_3\text{-C})_3$	−964	0	−862	0	4.47	0.02	1.61
5/3B	D_{3h}	D_{3h}	D_{3h}	$(\mu_4\text{-C})_3$	−907	57	−808	54	4.38	0.05	0.18
5/6A	C_2	C_{2v}	D_{3h}	$(\mu_3\text{-C})_6$	−1399	0	−1277	0	6.89	0.41	0.32
5/6B	C_2	C_{2v}	D_{3h}	$(\mu\text{-C}_2)_3$	−1370	29	−1254	23	4.08	0.59	0.67
6/6A	C_1	C_{2v}	D_{2h}	$(\mu_3\text{-C})_4(\mu_4\text{-C})_2$	−1573	0	−1462	0	5.25	0.74	0.2
6/6B	C_2	D_3	D_{3d}	$(\mu_3\text{-C})_6$	−1529	44	−1427	35	4.47	0.19	0.04
6/6C	C_2	C_2	?D_{3d}	$(\mu_4\text{-C}_2)_3$	−1508	65	−1401	61	4.73	0.74	0.2
6/6D	D_{2h}	D_{2h}	D_{2h}	$(\mu_4\text{-C}_2)_2(\mu_4\text{-C})_2$	−1472	101	−1374	88	4.25	0.14	0.2
6/7A	C_1	C_{2v}	C_{2v}	$(\mu_3\text{-C})_4(\mu_4\text{-C})(\mu_4\text{-C}_2)$	−1757	0	−1645	0	5.25	0.68	1.32
6/7B	C_1	C_{2v}	C_{2v}	$(\mu_3\text{-C})_4(\mu_4\text{-C})(\mu_4\text{-C}_2)$	−1746	11	−1622	23	5.59	0.93	0.37
6/7C	C_1	C_1	C_1	$(\mu_3\text{-C})_3(\mu_4\text{-C})_2(\mu_3\text{-C}_2)$	−1737	20	−1620	25	5.42	0.12	0.45
6/7D	C_{2v}	C_{2v}	C_{2v}	$(\mu_4\text{-C}_3)(\mu_4\text{-C})_2(\mu_3\text{-C})_2$	−1701	56	−1589	56	4.99	0.39	0.45
6/7E	C_1	C_1	C_3	$(\mu_4\text{-C}_2)_3(\mu_3\text{-C})$	−1688	69	−1575	70	5.03	0.23	0.33
6/7F	C_s	C_s	C_s	$(\mu_3\text{-C})_6(\mu_3\text{-C})$	−1660	97	−1562	83	4.94	0.06	0.4
6/7G	C_{2h}	D_3	D_{3d}	$(\mu_3\text{-C})_6(\mathrm{C}_{\mathrm{central}})$	−1623	134	SCF[g]			0.03	
6/7H	C_2	C_2	D_{3d}	$(\mu_4\text{-C}_2)_3(\mathrm{C}_{\mathrm{central}})$	−1618	139	−1502	143	5.07	0.03	0.08
6/7I	D_{2h}	D_{2h}	D_{2h}	$(\mu_4\text{-C})_2(\mu_3\text{-C})_4(\mathrm{C}_{\mathrm{central}})$	−1579	178				0.03	
6/8A	C_1	D_3	D_{3d}	$(\mu_4\text{-C}_2)_3(\mu_3\text{-C})_2$	−1888	0	−1758	0	5.81	0.01	0.65
6/8B	C_2	D_{2h}	D_{2h}	$(\mu_3\text{-C})_4(\mu_4\text{-C}_2)_2$	−1883	5	−1773	−15	5.07	0.04	0.29
6/8C	C_1	C_1	C_s	$(\mu_3\text{-C})_8$	−1794	94	−1703	55	5.59	0.48	0.42
6/8D	D_{2h}	D_{4h}	D_{4h}	$(\mu_4\text{-C}_2)_4$	−1785	103	−1676	82	5.38	0.12	0.18
6/8E	D_{2h}	O_h	O_h	$(\mu_3\text{-C})_8$	−1719	169	−1592	166	5.55	0.21	0.03
7/9A	C_1	C_s	C_{3v}	$(\mu_3\text{-C})_3(\mu_4\text{-C}_2)_3$	−2197	0	−2081	0	5.29	0.21	0.39
7/9B	C_s	C_s	C_{3v}	$(\mu_3\text{-C})_3(\mu_4\text{-C}_2)_3$	−2190	7	−2075	6	5.20	0.47	0.44
7/9C	C_{2v}	C_{2v}	C_{2v}	$(\mu_3\text{-C})_8(\mathrm{C}_{\mathrm{central}})$	−2084	113	−1938	143	6.11	0.5	0.05
8/12A	D_2	T_d	T_d	$(\mu_4\text{-C}_2)_6$	−2828	0	−2714	0	5.29	0.4	0.36
8/12B	C_{2v}	C_{2v}	C_{2v}	$(\mu_4\text{-C}_2)_6$	−2826	2	−2711	3	5.12	0.21	0.35
8/12C	C_1	D_{3d}	D_{3d}	$(\mu_4\text{-C}_2)_6$	−2809	19	−2687	27	5.42	0.43	0.34
8/12D	C_s	C_s	C_s	$(\mu_4\text{-C}_2)_6$	−2807	21	−2680	34	5.64	0.44	0.42
8/12E	D_2	D_{2d}	D_{2d}	$(\mu_4\text{-C}_2)_6$	−2786	42	−2655	59	5.77	0.45	0.23
8/12F	C_{2v}	D_{2h}	D_{2h}	$(\mu_4\text{-C}_2)_4(\mu_3\text{-C})_4$	−2785	43	−2663	51	5.42	0.81	0.81
8/12G	C_1	C_{3v}	C_{3v}	$(\mu_4\text{-C}_2)_6$	−2782	46	−2659	55	5.51	0.25	0.24
8/12H	C_{2h}	D_{3d}	D_{3d}	$(\mu_4\text{-C}_2)_6$	−2778	50	−2655	59	5.81	0.11	0.08
8/12I	D_2	D_2	D_2	$(\mu_4\text{-C}_2)_6$	−2774	54	−2655	59	5.29	0.45	
8/12J	D_2	D_2	D_2	$(\mu_5\text{-C}_3)_4$	−2596	232	−2509	205	5.07	0.31	0.19
8/12K	D_{2h}	T_h	T_h	$(\mu_4\text{-C}_2)_6$	−2593	235	−2480	234	4.90	0.09	0.33
8/12L	D_{3d}	D_{3d}	D_{3d}	C_{12}	−2492	336	−2383	331	4.73	0.31	0.41
8/12M	D_{2h}	O_h	O_h	$(\mu\text{-C})_{12}$	−2402	426	−2303	411	4.51	0.57	0.52
8/12N	D_{2h}	T_h	T_h	C_{12}	8/12K[e]		8/12K[e]				
8/12O	O_h	O_h	O_h	C_{12}	8/12M[e]		8/12M[e]				
8/12P	D_{2h}	T_h	T_h	$(\mu_4\text{-C}_2)_6$	8/12K[e]		8/12K[e]				
8/13A	T_d	T_d	T_d	$(\mu_4\text{-C}_2)_6(\mathrm{C}_{\mathrm{central}})$	−2963	0	−2853	0	4.90	0.06	0.27
9/8A	C_{2v}	C_{4v}	C_{4v}	$(\mu_3\text{-C})_4(\mu_4\text{-C})_4$	−2256	0	−2154	0	4.51	0.14	0.82
9/8B	C_{2v}	C_{2v}	C_{4v}	$(\mu_4\text{-C}_2)_4$	−2148	108	−2027	127	5.25	0.25	0.53
9/8C	C_{2v}	C_{4v}	C_{4v}	$(\mu_3\text{-C})_8$	−2085	171	−1948	206	5.90	0.18	0.33
9/9A	C_1	C_{4v}	C_{4v}	$(\mu_4\text{-C})_5(\mu_3\text{-C})_4$	−2472	0	−2368	0	4.86	0.52	0.61
9/9B	C_{2v}	C_{4v}	C_{4v}	$(\mu_4\text{-C}_2)_4(\mu_4\text{-C})$	−2319	153	−2210	158	4.77	0.12	0.11
9/9C	C_{2v}	C_{2v}	D_{3h}	$(\mu_3\text{-C})_6(\mu_4\text{-C})_3$	−2406	66	−2196	172	4.77	0.16	0.41
9/10A	C_s	C_s	C_s	$(\mu_3\text{-C})_4(\mu_4\text{-C})_4(\mu_4\text{-C}_2)$	−2617	0	−2512	0	4.68	0.27	0.49
9/10B	C_{2v}	C_{2v}	C_{2v}	$(\mu_3\text{-C})_4(\mu_4\text{-C})_2(\mu_4\text{-C}_2)_2$	−2578	39	−2472	40	4.68	0.1	0.65

TABLE 1. (Continued)

	symmetry			distribution of C atom types	binding energies (kcal mol^{-1})					HOMO−LUMO gap (eV)	
					neutral		cation				
isomer	const[b]	actual[c]	ideal[d]		BE(0)[e]	ΔBE(0)[e]	BE(+)[e]	ΔBE(+)[e]	IE (eV)	neutral	cation
9/10C	C_{2v}	C_{2v}	C_{2v}	$(\mu_3\text{-C})_4(\mu_4\text{-C})_2(\mu_4\text{-C}_2)_2$	−2546	71	−2438	74	5.03	0.02	0.16
9/10D	C_{2v}	C_{2v}	C_{2v}	$(\mu_4\text{-C}_2)_5$	−2517	100	−2376	136	5.38	0.15	0.01
10/12A	C_{2v}	C_{4v}	C_{4v}	$(\mu_4\text{-C}_2)_4(\mu_4\text{-C})_4$	−3057	0	−2952	0	4.73	0.05	0.16
10/12B	C_s	C_s	C_{3v}	$(\mu_4\text{-C}_2)_3(\mu_4\text{-C})_3(\mu_3\text{-C})_3$	−3050	7	−2929	23	5.38	0.11	0.12
10/12C	C_s	C_{3v}	C_{3v}	$(\mu_4\text{-C}_2)_3(\mu_4\text{-C})_3(\mu_3\text{-C})_3$	−3043	14	−2922	30	5.33	0.41	0.54
10/12D	C_1	C_3	C_3	$(\mu_4\text{-C}_2)_6$	−2944	113	−2845	107	4.55	0.07	0.24
10/12E	D_2	D_2	D_2	$(\mu_3\text{-C})_4(\mu_4\text{-C}_2)_4$	−2913	144	−2789	163	5.64	0.1	0.1
10/12F	C_1	C_{4v}	C_{4v}	$(\mu\text{-C})_4(\mu_3\text{-C})_4(\mu_4\text{-C})_4$	−2795	262	−2796	156	4.99	0.04	0.32
10/16A	C_{2v}	C_{2v}	C_{2v}	$(\mu_4\text{-C}_2)_8$	−3674	0	−3545	0	5.72	0.49	0.31
10/16B	C_{2v}	D_{4d}	D_{4d}	$(\mu_4\text{-C}_2)_8$	−3590	84	−3464	81	5.55	0.05	0.02
11/13A	C_1	C_{3v}	C_{3v}	$(\mu_4\text{-C})_6(\mu_3\text{-C})(\mu_4\text{-C}_2)_3$	−3311	0	−3209	0	4.42	0.07	0.17
11/15A	C_{2v}	C_{2v}	D_{3h}	$(\mu_4\text{-C}_2)_6(\mu_4\text{-C})_3$	−3713	0	−3593	0	5.33	0.12	0.06
11/15B	C_{2v}	C_{2v}	D_{3h}	$(\mu_4\text{-C}_2)_6(\mu_4\text{-C})_3$	−3683	30	−3579	14	4.68	0.23	0.15
11/15C	C_s	C_s	C_{3v}	$(\mu_4\text{-C}_2)_6(\mu_4\text{-C})_3$	−3691	22	−3577	16	4.94	0.12	0.26
12/12A	C_{2h}	C_{2h}	C_{2h}	$(\mu_3\text{-C})_4(\mu_4\text{-C})_8$	−3338	0	−3236	0	4.68	0.34	0.1
12/12B	C_{2h}	D_{3d}	D_{3d}	$(\mu_3\text{-C})_6(\mu_4\text{-C})_6$	−3248	90	−3135	101	4.99	0.15	0.23
12/12C	D_{3d}	D_{3d}	D_{3d}	$(\mu_3\text{-C})_6(\mu_4\text{-C})_6$	−3235	103	−3127	109	4.86	0.08	0.09
12/12D	D_2	T_h	T_h	$(\mu_4\text{-C}_2)_6$	−3191	147	−3076	160	5.46	0.31	0.17
12/14A	D_2	O_h	O_h	$(\mu_4\text{-C})_6(\mu_3\text{-C})_8$	−3555	0	−3423	0	5.77	0.03	0.03
12/14B	C_i	S_6	S_6	$(\mu_4\text{-C}_2)_6(\mu_3\text{-C})_2$	−3479	76	−3354	69	5.55	0.29	0.25
12/15A	C_{2v}	C_{2v}	C_{3v}	$(\mu_4\text{-C}_2)_6(\mu_5\text{-C})_3$	−3725	0	−3626	0	4.38	0.16	0.15
12/15B	C_1	C_1	C_3	$(\mu_4\text{-C}_2)_6(\mu_3\text{-C})_3$	−3629	96	−3499	127	5.72	0.15	0.22
12/15C	C_{2v}	C_{2v}	C_{2v}	$(\mu_3\text{-C})_4(\mu_4\text{-C})_5(\mu_5\text{-C}_3)_2$	−3601	124	−3514	112	4.86	0.01	0.11
12/15D	C_1	D_{2h}	O_h	$(\mu_4\text{-C})_6(\mu_3\text{-C})_8(\mathrm{C}_{\mathrm{central}})$	−3541	184	−3435	191	5.94	0.01	0.02
12/20A	D_2	D_2	D_{2h}	$(\mu_4\text{-C}_2)_6(\mu_3\text{-C})_8$	−4160	0	−4031	0	5.76	0.03	0.2
14/14A	D_{2h}	D_{2h}	D_{2h}	$(\mu_4\text{-C})_{10}(\mu_4\text{-C}_2)_2$	−3959	0	−3869	0	3.95	0.11	0.13
14/14B	C_{2v}	C_{2v}	C_{2v}	$(\mu_4\text{-C})_{10}(\mu_4\text{-C}_2)_2$	−3916	43	−3820	49	6.29	0.13	0.13
14/15A	D_{2h}	D_{2h}	D_{2h}	$(\mu_4\text{-C})_{10}(\mu_4\text{-C}_2)_2$ $(\mathrm{C}_{\mathrm{central}})$	−4129	0	−4037	0	3.99	0.12	
14/16A	D_{2h}	D_{2h}	D_{2h}	$(\mu_4\text{-C})_8(\mu_4\text{-C}_2)_4$	−4222	0	−4133	0	3.90	0.1	0.1

[a] Within each composition (*x*/*y*) group, the isomers are arranged in order of decreasing stability of the neutral cluster. Energies are internal energies, without zero-point or thermal corrections. [b] Point group symmetry constraint used during exploration of the optimized structure. [c] Actual point group symmetry of the molecule. [d] Highest idealized point group symmetry. [e] BE(0) and BE(+) are the cluster binding energies for neutral and cation respectively: ΔBE(0) and Δ*BE*(+) are cluster binding energies relative to the most stable isomer. [f] Optimization yielded this structure. [g] SCF convergence could not be achieved.

energies (IE) are vertical and calculated as the difference in energy between the optimized neutral and the cation at the geometry of the neutral. Atom coordinates for all structures are available as Supporting Information.

Results

The results are organized by increasing cluster size, which is useful because smaller clusters are often the fragments that constitute larger clusters. Isomeric structures for the composition Nb_xC_y (abbreviated as *x*/*y*) are labeled as ***x*/*y*A**, ***x*/*y*B**, ***x*/*y*C**, etc. Isomer labeling within each composition is alphabetical in order of more positive energy for the neutral cluster. In the figures presenting all of the isomers, Nb−Nb bonds are drawn when the distance is less than 2.55 Å; even though there might be a considerable Nb−Nb bonding interaction at longer distances, this short distance is chosen to simplify the figures and to emphasize the Nb−C and C−C bonding which we consider to be more significant. However, one consequence of the non-representation of Nb−Nb > 2.55 Å is that some Nb atoms in the figures appear to be undercoordinated, even though there are additional Nb−Nb interactions. Important Nb−Nb distances are given in the figures or in their captions. The figures give the neutral energies relative to the most stable isomer for each composition.

Details for each of the 100 structures calculated are given in Table 1. In some cases, the HOMO−LUMO gap is small, and the structure has close-lying excited states. Full details of electronic structure with unrestricted calculations are not reported in this paper, which aims to identify the broad structural principles and to first paint the bigger picture of Nb_xC_y clusters.

To compare clusters with different compositions, and to obtain information on absolute stabilities, we calculate and report normalized binding energies. BE′ is the binding energy per atom, and BE″ is the binding energy per valence electron, with four electrons counted for C and five for Nb.

Nb_2C_2. The energy minima for this composition are pictured in Figure 2. The most stable structure found is the planar **2/2A**, which consists of a Nb_2 unit (the Nb−Nb distance is 2.72 Å in **2/2A^0** and 2.73 Å in **2/2A$^+$**) bridged by two carbon atoms, with Nb−C distances of 1.94 Å in both the neutral and the cation. The minimal difference in geometry between the **2/2A^0** and the **2/2A$^+$** suggests that the nondegenerate HOMO of the neutral (which is also the singly occupied HOMO of the cation) is nonbonding in character. The calculated ionization energy of 6.3 eV is high in comparison with the IEs of many of the larger Nb_xC_y structures. **2/2B^0** containing a C_2 unit bridging a Nb−Nb bond is found to be 8 kcal mol^{-1} higher in energy than **2/2A^0**, while **2/2B$^+$** is 19 kcal mol^{-1} higher in energy than **2/2A$^+$**. The Nb−Nb distance in **2/2B^0** is short, at 2.29 Å (2.35 Å in **2/2B$^+$**), much shorter than that for **2/2A**. The linear isomer **2/2C** is not energetically competitive, and **2/2C$^+$** is not stable, as Nb−Nb bond breakage occurs without a barrier. The alternative postulated structure in which a C_2 bond is perpendicular to a Nb−Nb bond (an irregular tetrahedron of atoms) optimized to **2/2B**. Nonplanar versions of **2/2A** occur on a relatively flat energy surface with a minimum at planar **2/2A**.

It seems that, for Nb_2C_2, stability is maximized with the number of Nb−C bonds, as in **2/2A**. A reduction of Nb−C bonding to increase C−C and Nb−Nb bonding, as in **2/2B** and **2/2C**, is not stabilizing.

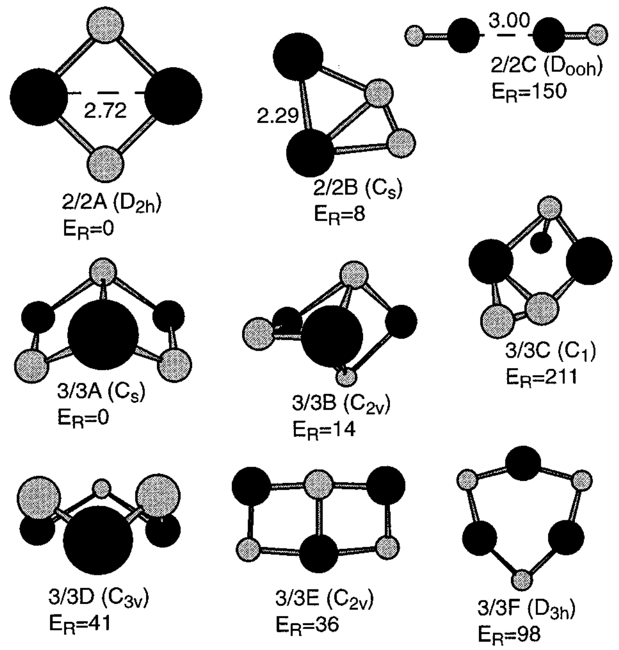

Figure 2. Optimized isomers of Nb_2C_2 and Nb_3C_3. Nb atoms are black, C atoms are speckled, and point-group labels give the idealized symmetry. The relative energy E_R is the binding (internal) energy (kcal mol^{-1}) of the isomer (as the neutral) referenced to the most stable isomer for that composition. Interatomic distances, where given, are in Å.

Nb_3C_3. Of the six isomers of 3/3 (see Figure 2), two have Nb_3 as an equilateral triangle and four as an isosceles triangle; the differences between the isomers are in the types and locations of C atoms. Only **3/3C** has a C−C bond. The most stable isomer is **3/3A** (C_s), which contains $(\mu_3\text{-C})_1(\mu\text{-C})_2$ bridges to an approximately equilateral Nb_3 triangle. The alternative bridging, $(\mu_3\text{-C})_2(\mu\text{-C})_1$ in **3/3B**, is destabilized by 14 kcal mol^{-1} for the neutral (17 kcal mol^{-1} for **3/3B**$^+$), possibly because of the close proximity of the two μ_3-C atoms [$(\mu_3\text{-C})\cdots(\mu_3\text{-C})$ is less than 2.8 Å for both **3/3B**$^+$ and **3/3B**^{0}]. The Nb−C distances of **3/3A** are essentially unchanged between the two charge states, as $(\mu_3\text{-C})$−Nb = 2.10 Å and $(\mu\text{-C})$−Nb = 1.90 Å. The Nb−Nb distances in **3/3A**^{0} are 2.85 and 2.89 Å, contracting to 2.83 Å in **3/3A**$^+$, which suggests a slight Nb−Nb antibonding character of the **3/3A**^{0} HOMO (LUMO of **3/3A**$^+$). Both the HOMO and the LUMO of **3/3A**$^+$ consist mostly of contributions from the 4d and 5s atomic orbitals of Nb. Structures with different bridging qualities are considerably less stable. All of the isomers considered for 3/3 contain three Nb−Nb distances of between 2.6 and 3.1 Å, except for **3/3E**, which has only two such Nb−Nb distances (ca. 2.9 Å). Folding **3/3E** along the 2-fold axis shortens one Nb−Nb distance and leads to the energy minimum of **3/3A**.

The high-symmetry (D_{3h}) isomer **3/3F** is not stable. Displacement of the carbon atoms by only 0.1 Å out of the plane followed by optimization leads to the **3/3D** isomer, and it is notable that the energy difference between **3/3D**$^+$ and **3/3F**$^+$ is more than 70 kcal mol^{-1}.

Like **3/3A**, **3/3D** can be considered as a depleted 2 × 2 × 2 nanocrystallite; **3/3E** can be considered as the regular 3 × 2 × 1 nanocrystallite, whereas **3/3B**, **3/3C**, and **3/3F** are not easily recognized as fragments of the cubic crystal lattice.

Nb_3C_4 and Nb_4C_3. Both **3/4A** and **4/3A** are irregular nanocrystallite fragments derived from cubanoid **4/4A** (the 2 × 2 × 2 nanocrystallite) by removal of a Nb atom or a C atom, respectively. The minimized geometries are shown in Figure 3.

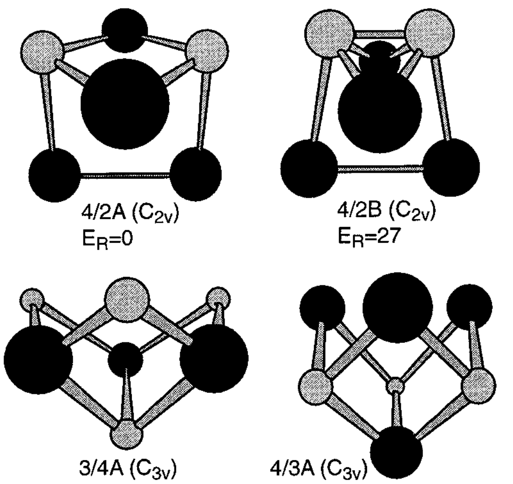

Figure 3. Optimized isomers of Nb_4C_2, Nb_3C_4, and Nb_4C_3. Symbols as in Figure 2.

Nb_4C_2. The two structures evaluated for 4/2 are shown in Figure 3. Both consist of a tetrahedron of Nb atoms, **4/2A** with two Nb_3 faces capped by carbon atoms and **4/2B** with the two carbon atoms brought to within bonding distance. **4/2B** is not a local energy minimum, and optimization breaks the C−C bond, leading to **4/2A**. The Nb−Nb distances for **4/2A**^{0} range from 2.40 to 2.86 Å, while the Nb−C distances are 2.02 and 2.29 Å. The shorter Nb−Nb distances in **4/2A**^{0} lengthen by about 0.05 Å in **4/2A**$^+$, indicating that the HOMO is slightly Nb−Nb bonding in character. For this composition with $y/x < 1$, it appears that Nb−C bonding contributes more to stability than C−C bonding. **4/2A** is another example of a depleted 2 × 2 × 2 nanocrystallite.

Nb_4C_4. Eight structures calculated for 4/4 are shown in Figure 4. The cubanoid structure **4/4A**, which is clearly the most stable isomer, is also the archetypal 2 × 2 × 2 nanocrystallite fragment. Isomer **4/4C**, also a nanocrystallite fragment but with two fewer Nb−C bonds, is 60 kcal mol^{-1} less stable. Structure **4/4D** is a fusion of two M_4C_2 cradles (see below), which are the key C_2 binding motif in $Ti_8(C_2)_6$,[54,81] and as such **4/4D** was expected to be more competitive, but is 68 kcal mol^{-1} less stable than **4/4A**. We believe that the reason for this is that the Nb−C−C angles involving the Nb atoms at the end of each cradle are too acute, diminishing the C−C−Nb σ bonding. A similar destabilizing effect occurs in **4/4B**. Structures **4/4E** and **4/4F** with undercoordinated C_2 groups are quite unfavorable, while the planar isomers **4/4G** (with C atoms) and **4/4H** with C_4 are worse. Structures that contain short Nb−Nb distances at the expense of Nb−C bonds are energetically unfavorable.

For **4/4A**^{0}, there is a slight (<0.01 Å) distortion from the optimal T_d symmetry to D_{2d}, but there is no obvious electronic reason for this, and the energetic stabilization associated with the distortion is less than 1 kcal mol^{-1}. This distortion is somewhat more marked (0.05 Å) in the cation, as evidenced by the variation in both the Nb−Nb distances (four at 2.96 Å, two at 2.91 Å) and the Nb−C distances (eight at 2.07 Å, four at 2.02 Å). Calculated vibrational frequencies show that **4/4A**^{0} is a minimum on the local energy hypersurface. The Nb−Nb distances in the neutral are two at 2.947 Å and four at 2.953 Å, and the Nb−C distances range between 2.055 and 2.059 Å. Our DF-calculated **4/4A**^{0} geometry compares well with that calculated by Freiser et al,[47] who carried out calculations at the closed-shell Hartree−Fock level on $Nb_4C_4°$ using an effective relativistic core potential for Nb and double-ζ basis sets for Nb and C (6-31G); they report Nb−Nb distances of 2.96 Å and

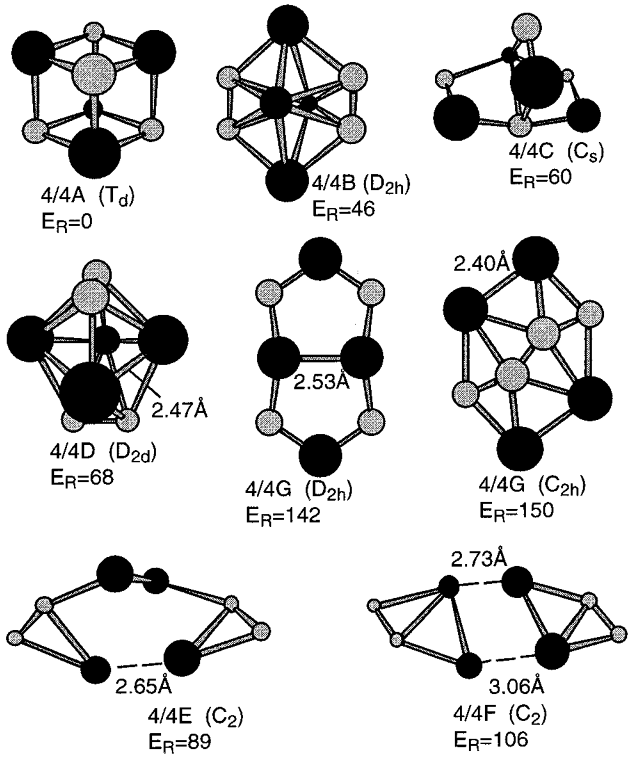

Figure 4. Optimized isomers of Nb_4C_4. Symbols as in Figure 2. Significant Nb−Nb distances are as follows: **$4/4A^0$**, 2.95 Å; **$4/4^+$**, four at 2.96 Å and two at 2.91 Å; **$4/4B^0$**, four at 2.51 Å and one at 2.85 Å; **$4/4B^+$**, four at 2.53 Å and one at 2.86 Å Significant angles are as follows: **$4/4A^0$**, Nb−C−Nb, 91.7° and C−Nb−C, 88.4°; **$4/4A^+$** Nb−C−Nb, eight at 92.7° and four at 89.2°, C−Nb−C, eight at 87.3° and four at 90.4°

Nb−C distances of 2.01 Å. They did not recognize any distortion from T_d, as their optimization was constrained to that symmetry.

The HOMO−LUMO gaps for both **$4/4A^+$** (0.31 eV) and **$4/4A^0$** (0.27 eV) are smaller than those for the stable isomers of smaller clusters, namely, **$2/2A^0$** = 0.54 eV, **$3/3A^0$** = 0.37 eV (see Table 1). For **$4/4A^0$**, the binding energy per atom (BE′ = −126 kcal mol^{-1} $atom^{-1}$) and the binding energy per valence electron (BE″ = −28.0 kcal mol^{-1} e^{-1}) are both larger than any values calculated for smaller structures. The ionization energy of **4/4A** at 5.12 eV continues a trend of decreasing IE with increasing cluster size (**2/2A**, 6.33 eV; **3/3A**, 5.59 eV). The high stability and low ionization energy calculated for **4/4A** in comparison with those for smaller structures indicates that this species should show strong abundance in this region of the mass spectra, which is indeed the case.[30]

Figure 5 shows part of the MO diagram for **$4/4A^0$**. The HOMO is more than 2 eV higher in energy than the next-highest-occupied molecular orbital (NHOMO) and is doubly degenerate. The LUMO is triply degenerate, and its proximity to the HOMO allows many low-lying excited spin states.

One of the questions for Nb_xC_y clusters concerns the magnitude of Nb−Nb bonding energy relative to Nb−C bond energy. One way to estimate this issue is to explore symmetrical breathing distortions of a structure such as **$4/4A^0$**, in which the Nb−Nb distance can vary with relatively minor angular distortions. Therefore, we calculated the energies of **$4/4A^0$** with Nb−Nb lengthened or shortened by 0.2 Å and the Nb−C distance unchanged. Shortening Nb−Nb to 2.75 Å costs 32 kcal mol^{-1}, and lengthening to 3.15 Å costs 35 kcal mol^{-1}. Although these are upper bounds for Nb−Nb energies, it appears that there are significant Nb−Nb contributions to the cluster energy even at Nb−Nb = 2.95 Å.

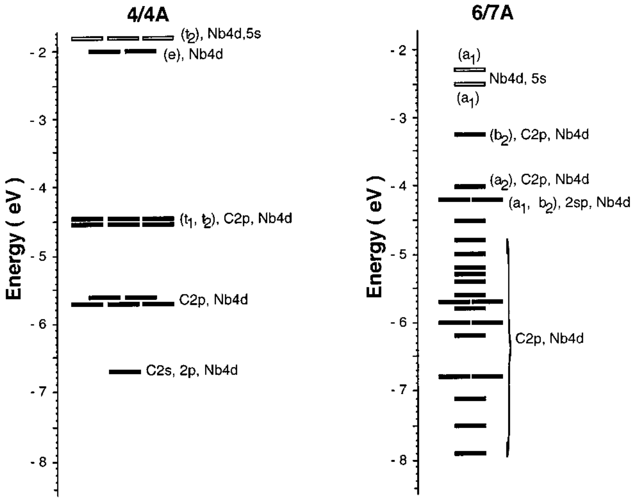

Figure 5. Calculated electronic structures of **$4/4A^0$** and **$6/7A^0$**. Significant atomic orbital contributions to molecular orbitals are shown to the right of each MO. Filled rectangles represent occupied orbitals; open rectangles represent unoccupied orbitals. Symmetries of selected orbitals are given.

Nb_5C_3. Isomer **5/3A**, shown in Figure 6, is generated by replacing one C atom of the cubanoid **4/4A** with Nb. This C_{3v} structure distorts to C_s on optimization. Interatomic distances are given in Figure 6. The calculated stability of **5/3A**, a substituted nanocrystallite, in relation to **5/3B** suggests that minor substitution of atoms in nanocrystallites is energetically feasible. Isomer **5/3B** is a trigonal bipyramid of Nb atoms with a C atom between each pair of equatorial Nb atoms and D_{3h} symmetry, but it is much higher in energy than **5/3A**.

Nb_5C_6. Two related structures with a trigonal bipyramid of Nb atoms were evaluated for 5/6 (see Figure 6). Isomer **5/6A** has a single carbon atom capping each Nb_3 face, whereas **5/6B** contains three C−C bonds. **5/6A** is more stable than **5/6B** as either the neutral (29 kcal mol^{-1}) or the cation (23 kcal mol^{-1}). Both **$5/6A^0$** and **$5/6A^+$** are calculated to have only C_{2v} symmetry instead of the idealized D_{3h} symmetry. Nb^{eq}−Nb^{eq} distances in **$5/6A^+$** are one at 2.68 Å and two at 2.95 Å, Nb^{ax}−Nb^{eq} distances are four at 3.03 Å and two at 3.00 Å, while Nb−C distances range from 1.97 to 2.33 Å, and C−C distances are greater than 3 Å. The occurrence of three C−C bonds in **5/6B** causes the extension of three Nb^{eq}−Nb^{eq} distances to more than 3.6 Å. Breaking three Nb−Nb bonds to form three C−C bonds could be expected to stabilize **5/6B** over **5/6A**, but the calculated reverse energy ordering of these two isomers is believed to be a consequence of the stereochemistry at the C atoms. In **5/6A**, each C atom has three σ C−Nb bonds in a trigonal pyramidal arrangement. However, in **5/6B**, both the σ and π interactions of the C_2 acetylide group are distorted: the Nb^{ax}−C−C angle is only 123°, destabilizing the overlap of the C−C σ^* orbitals with Nb^{ax}, and the overlap of the π orbitals of C_2 with Nb^{eq} is also unfavorable because the Nb^{eq}−(C_2)−Nb^{eq} angle is near 120° rather than the ideal 90°. Both the HOMO and the LUMO in **$5/6A^+$** consist mostly of Nb 4d and Nb 5s atomic orbital contributions, and the HOMO of the neutral is bonding with respect to the Nb^{eq}−Nb^{eq} bonds, which lengthen by more than 0.2 Å on ionization.

Nb_6C_6. The four isomers considered for 6/6 are shown in Figure 6. The most stable isomer, **6/6A**, is based on two cubane units (**4/4A**) fused together, whereas **6/6B** is a stacked pair of Nb_3C_3 rings. **6/6B** is 44 and 35 kcal mol^{-1} higher in energy

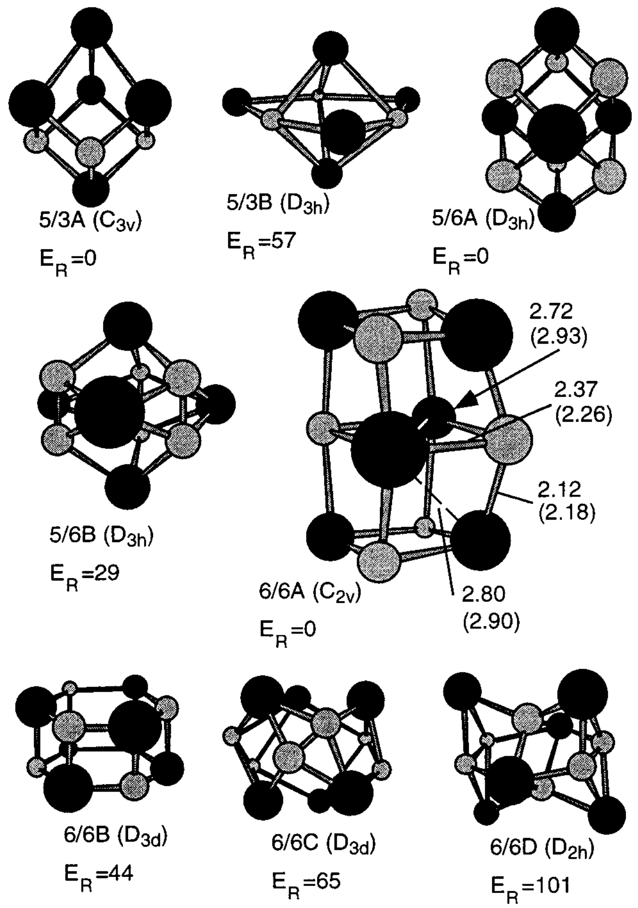

Figure 6. Optimized isomers of Nb_5C_3, Nb_5C_6 and Nb_6C_6. Symbols as in Figure 2. The mirror plane of **5/3A** is perpendicular to the page. Interatomic distances are in Å where given; distances for the neutral are given first, with the cation distances in parentheses. In **5/3B**, $Nb^{ax}-Nb^{eq}$ is 2.74 Å in both the cation and the neutral; $Nb^{ax}-Nb^{ax}$ is 3.04 Å in the neutral and 2.96 Å in the cation. Interatomic distances (Å) for neutral **6/6A** are given in the figure, with distances for the cation given in parentheses.

than **6/6A** as the neutral and monocation, respectively. Isomer **6/6C** is a less stable derivative of **6/6B** containing three C−C bonds, and **6/6D**, with two C−C bonds, is even less stable. **6/6B** is related to **6/6A** by expansion of two parallel Nb−C diagonals in the Nb_3C_3 rings. Although **6/6A** could have D_{2h} symmetry, the optimized structure is C_{2v} with one Nb−C−Nb approximately linear edge being different from the other. Selected distances for **6/6A** as the neutral and monocation (in parentheses) are shown in Figure 6. It is noted that marked distances lengthen by as much as 0.2 Å on ionization, indicating that the HOMO is significantly bonding with respect to all of the bonds shown. Little variation is seen in other distances in the molecule for this electron removal. The HOMO of **6/6A** shows major contributions from Nb 4d and C 2p atomic orbitals, whereas the LUMO shows contributions only from Nb 4d and Nb 5s. A frequency calculation performed on **6/6A^0** showed only real frequencies, indicating this to be a minimum on the energy hypersurface.

Structure **6/6B** can be puckered in two ways to form stacked chairs rather than stacked planes. As shown in Figure 7, both of these alternatives have been optimized, yielding isomers **6/6A** or **6/6B**.

At this stage, considering 4/4, 5/6, and 6/6, it is evident that the incorporation of C_2 groups in M_xC_y where $y/x \approx 1$ is destabilizing.

Nb_6C_7. This is an unusual and informative composition for metal−carbon clusters, and nine different structural isomers were evaluated for Nb_6C_7 (see Figure 8). Generation of favorable structures is accomplished by replacing a carbon atom in **6/6A** with a C_2 group. The most stable isomers, **6/7A**, **6/7B**, and **6/7C**, are formed in this fashion. The increased stability of **6/7A** over **6/7B** can be attributed to an increased bonding interaction between the two central Nb atoms, resulting in this Nb−Nb distance decreasing from 2.98 Å in **6/7B^0** to 2.52 Å in **6/7A^0**. In isomer **6/7C**, the C_2 group replaces a μ_3-C of **6/6A** rather than a μ_4-C atom. Isomer **6/7D** is derived from **6/6A** with a C_3 group capping one end of the molecule, and the destabilization is consistent with results from many other met−cars, which indicate that C_3 groups are unfavorable. The remaining 6/7 isomers were generated either by adding a central carbon atom or by capping Nb_3 faces of various 6/6 structures. These strategies do not generate stable structures, particularly the inclusion of a high-coordinate central C atom in **6/7G**, **6/7H** and **6/7I**. Structure **6/7I**, originally proposed by Freiser et al.,[22] is a C-centered version of **6/6A**. When constrained to D_{2h} symmetry, this structure is almost 180 kcal mol^{-1} less stable than **6/7A**, whereas optimization without constraints yields **6/7B** with the formation of one C_2 unit.

A frequency calculation on **6/7A^0** confirmed that it is a true local energy minimum. Molecular orbitals for **6/7A** are shown in Figure 5. **6/7A** has a singly degenerate HOMO that consists mostly of Nb 4d and Nb 5s and less significant C 2p atomic orbital contributions. Not surprisingly, the electronic structure of **6/7B** is very similar to that of **6/7A**. Ionization causes little change in the geometry of **6/7A**, the only notable change being a slight (~0.05 Å) contraction of the central Nb−Nb distance on ionization. The HOMO can be considered as mostly nonbonding in character. The HOMO−LUMO gap for **6/7A$^+$** is large (1.32 eV) when compared with those of either **6/6A$^+$** (0.20 eV) or **6/7A^0** (0.68 eV).

At this point, it is useful introduce an important structural unit in met−car structures, the M_4C_2 cradle (see Figure 9), in which a C_2 group is bound along the long diagonal of an M_4 quadrilateral. Each C atom is bonded to three M atoms. The C_2 group has σ and π orbitals that define the two M^σ atoms near the ends of C_2 and the two M^π atoms transverse to C_2. A significant variable in the cradle unit is the concavity of the M_4 set. In conformer **1A**, the nonplanarity of M_4 is such that the $M^\sigma-C-C-M^\sigma$ atoms approach linearity and the $M^\pi-C_2-M^\pi$ set is near orthogonal. In the intermediate conformer **1B**, the M_4 set is planar. In **1C**, the folding of the M_4 set is the reverse of that in **1A**, causing increased bending of $M^\sigma-C-C$ and less bending of $M^\pi-C_2-M^\pi$. Although there are obvious bonding consequences within the cradle, the total energy of a met−car is influenced by additional factors, and the cradle motifs are employed mainly as an aid in the description of geometry in met−car structures. Structure **6/7A** contains one **1A**, and **6/7B** contains one **1C**. Isomer **4/4D**, described above, is believed to be unfavorable because it contains two **1C** cradles.

Nb_6C_8. The five structures investigated for 6/8 are presented in Figure 10. Isomers **6/8A** and **6/8B** are appreciably more stable than the others and have antecedents in earlier structures. **6/8A** is **6/6C** plus two μ_3-C caps, and **6/8B** is **6/6A** with the two central μ_4-C atoms replaced by C_2. There are some notable superficial anomalies: (1) Whereas the expansion of **6/6A** to **6/7A** yielded the most favorable structure for 6/7, continuation of this process to generate **6/8B** was not as competitive. (2) **6/6C** is not a favorable isomer for 6/6, single capping of **6/6C** to yield **6/7E** does not yield a good structure for composition

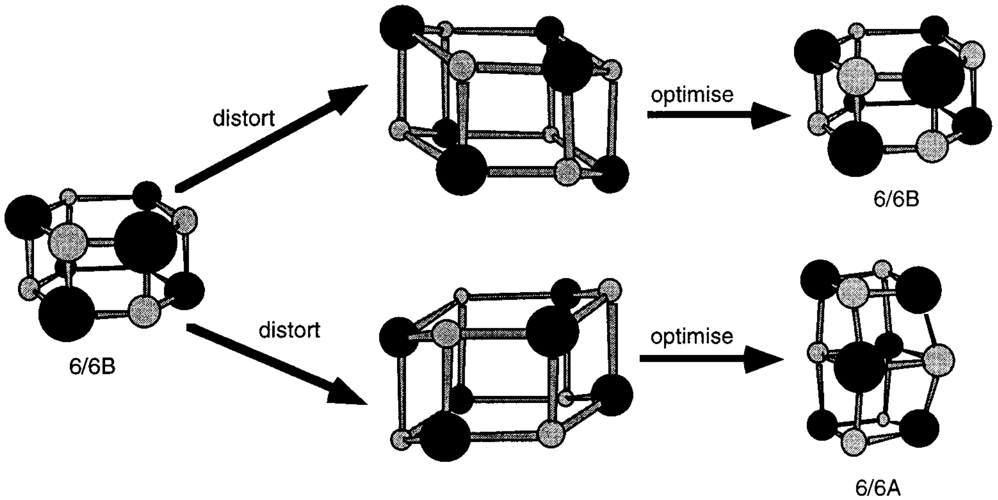

Figure 7. The two different chair distortions of structure **6/6B**, and the results of their optimization.

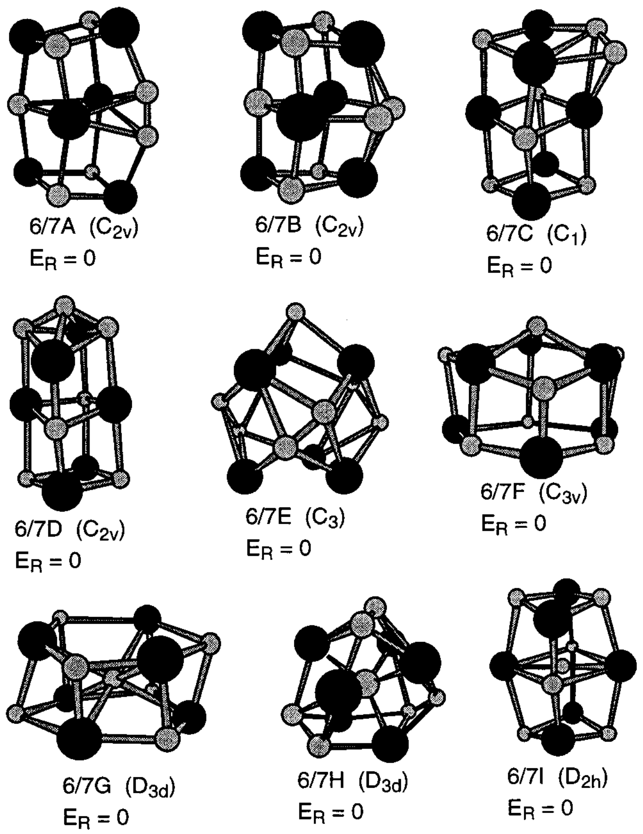

Figure 8. Optimized isomers of Nb_6C_7. Symbols as in Figure 2. Nb−Nb distances through the middle of **6/7A** and **6/7B** (perpendicular to the 2-fold rotational axis) are as follows: **6/7A^0** = 2.52 Å, **6/7A$^+$** = 2.98 Å; **6/7B^0** = 2.58 Å, **6/7B$^+$** = 2.94 Å.

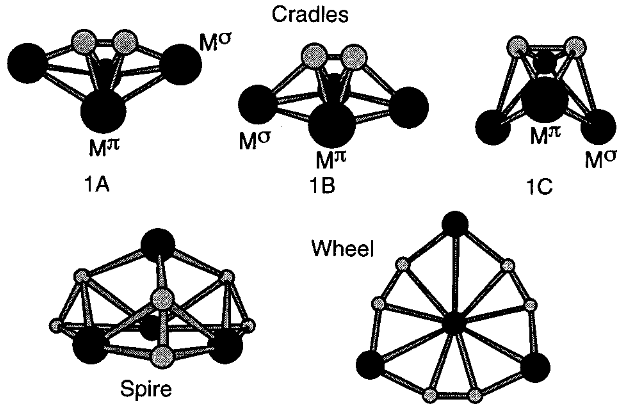

Figure 9. Cradle, wheel, and spire motifs commonly present in calculated Nb_xC_y structures.

6/7, but double capping of **6/6C** yields the most stable neutral isomer for composition 6/8. However, **6/8B$^+$** is 15 kcal mol^{-1} more stable than **6/8A$^+$**, and **6/8B** has a lower ionization energy than **6/8A**, so it is likely that the species observed mass spectrometrically is **6/8B$^+$**. The Nb−C distances from the central Nb atoms of **6/8B** to the surrounding C_2 groups contract by almost 0.1 Å on ionization, indicating that the HOMO is antibonding with respect to these Nb−C bonds.

For the composition 6/8, with an M/C ratio greater than one, it might be expected that favorable structures would contain some C_2 groups, and this is borne out by the results. Structures **6/8A** and **6/8E** have similar arrays of Nb and C atoms and differ mainly by the presence of three C−C bonds in **6/8A**; the formation of C−C bonds by **6/8E** was prevented by the D_{2h} symmetry used in its optimization, as the maximum symmetry of **6/8E** is O_h. The unusual isomer **6/8D** with C_4 cycles is energetically uncompetitive; from our investigations of other met−car structures, there is no indication that C_4 cycles are favorable.

Nb_7C_9. The three structures optimized for the composition 7/9 are pictured in Figure 10. Isomers **7/9A** and **7/9B** each contain three isolated C atoms and three C_2 groups, and they are much more stable than **7/9C**, which is composed of fused cubanoid units with C atoms only. This discussion focuses on **7/9A** and **7/9B** and the relationships between them. In both cases, the highest possible symmetry, C_{3v}, is reduced in the ground state to C_s, but it is useful to consider **7/9A** and **7/9B** in terms of their C_{3v} ideals. In **7/9A**, the Nb array is essentially a monocapped octahedron, whereas in **7/9B**, it is a tricapped tetrahedron. **7/9A** is elongated along its 3-fold rotation axis, with three C_2 groups aligned axially in type-**1A** cradles. In contrast, **7/9B** is compressed, with three C_2 groups perpendicular to the molecular 3-fold axis, also in type-**1A** cradles. There are also substantial differences in the bond angles at the C atoms. Despite these geometrical differences, the energies of the two isomers differ by only 7 kcal mol^{-1} for the neutral and 6 kcal mol^{-1} for the cation. The relationship between **7/9A** and **7/9B** can be described as a 90° rotation of the three C_2 groups.

Ionization of **7/9A^0** results in the contraction of the M^{π}−C distances, from approximately 2.35 to 2.25 Å, indicating that the HOMO is antibonding with respect to these bonds. The

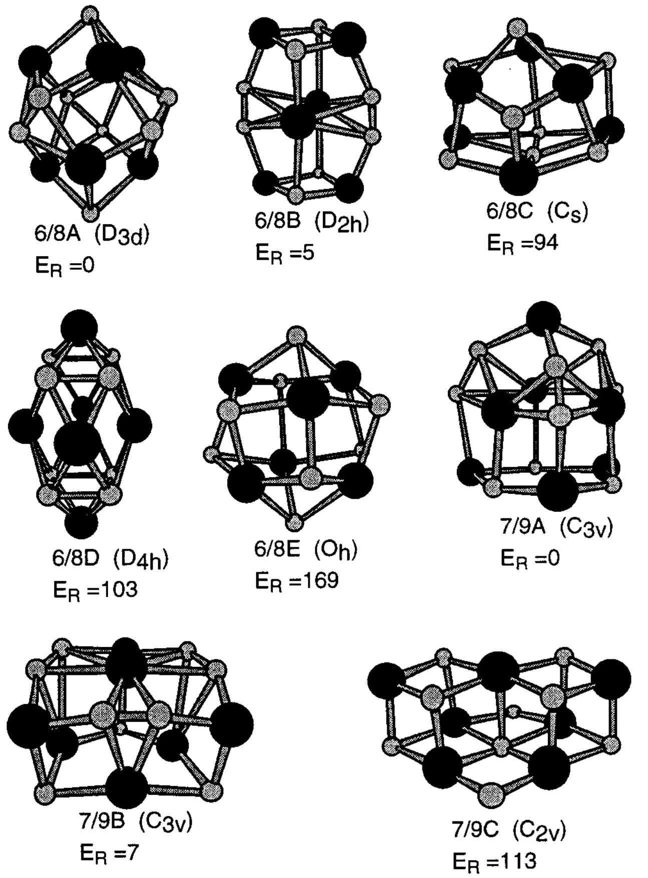

Figure 10. Optimized isomers of Nb_6C_8 and Nb_7C_9. Symbols as in Figure 2. Nb−Nb distances in the two Nb_3 triangles perpendicular to the pseudo-3-fold axis of **7/9A^0** (**7/9A$^+$**) are as follows: lower triangle, one at 2.9 Å (3.7 Å) and two at 3.1 Å (3.8 Å); upper triangle, one at 3.4 Å (3.2 Å) and two at 3.6 Å (2.9 Å). The remainder of the Nb−Nb distances in **7/9A** in both charge states range between 2.8 and 2.9 Å. Nb−C distances in **7/9A** are mainly invariant with charge state: $C^{isolated}$−Nb and C_2−Nb^{σ} range between 2.05 and 2.20 Å; however, the C_2−Nb^{π} distance increases from ca. 2.25 Å in the cation to ca. 2.35 Å in the neutral.

Nb^{π}−Nb^{π} distances show a marked change when the lone electron is removed from the HOMO of the neutral. Two of the Nb^{π}−Nb^{π} distances contract from more than 3.5 to about 2.95 Å, while the other shortens from 3.4 to 3.2 Å (the variation in these Nb−Nb distances for each charge state illustrates the major deviation from the ideal C_{3v} symmetry to C_s). However, it is noted that the potential energy curve for Nb−Nb > 3 Å is likely to be quite flat. In fact, the difference between the energy of **7/9A$^+$** at the geometry of **7/9A^0** and the ground-state energy of **7/9A$^+$** is only 6 kcal mol^{-1}.

Structures **7/9A** and **7/9B** demonstrate structural moieties that become prevalent in larger cluster structures: these are the $Nb_4(C_2)_3$ "spire" and the $Nb_4(C_2)_3$ "wheel" presented in Figure 9. The 3-fold spire is a tetrahedron of metal atoms elongated along one 3-fold axis, whereas the 3-fold wheel is compressed and almost planar $\{M^{\pi}(M^{\sigma})_3\}$. Isomer **7/9A** is a spire mounted on a Nb_3C_3 hexagon, whereas **7/9B** is a wheel attached to a Nb_3C_3 hexagon. Note that cradles of Figure 9 are generated only when the spire or wheel is bonded to other metal atoms.

Nb_8C_{12} and Nb_8C_{13}. Sixteen different structures were evaluated for the key composition 8/12, and they are pictured in Figure 11. Many of these isomers have been proposed previously for other M_8C_{12}, whereas some are entirely new possibilities. Our tetracapped tetrahedral (or bitetrahedron) structure **8/12A**,[54,81] now generally considered most probable for Ti_8C_{12},[56] is found also to be the most stable of the isomers of Nb_8C_{12}. This structure has four inner (Nb^{i}) and four outer (Nb^{o}) metal atoms. The isomers described by Benard[55] (**8/12A**−**E**, **H**, **I**), which include Chen's **8/12E**[82] and are generated by 90° rotations of the C_2 groups in **8/12A**, make up seven of the nine most stable isomers calculated for Nb_8C_{12}. Isomers **8/12B** and **8/12C** are quite close in energy to **8/12A**, being, respectively, 2 and 19 kcal mol^{-1} less stable as neutrals and 3 and 27 kcal mol^{-1} less stable as monocations. The more stable isomers of **8/12** can be described in terms of the motifs shown in Figure 9. **8/12A** consists of four fused wheels, or four fused spires, or a coaxial pairing of a wheel and a spire; **8/12B** contains two edge-shared wheels; **8/12C** is a fusion of two coaxial spires; **8/12D** contains a fused wheel and spire; and **8/12G** and **8/12H** consist of two coaxial wheels.

A new structure **8/12F**, which consists of two fused **6/8B** and contains a mix of isolated C atoms and C_2 groups, is calculated to have considerable stability, as is **8/12G**, which is a lower-symmetry version of **8/12H**.

Castleman's **8/12K**[11] is more than 230 kcal mol^{-1} higher in energy than **8/12A** as both the neutral and the monocation. Neither **8/12N** nor **8/12P**[83] corresponds to a minimum on the energy hypersurface, and when constrained to T_h symmetry both optimize to **8/12K**. **8/12O**[84] also does not correspond to a minimum on the energy surface, because optimization of this isomer yields the high-energy isomer **8/12M**, which is the only structure considered that contains only isolated C atoms.

Structures **8/12J** and **8/12L**,[85] with C chains longer than C_2, are calculated to have poor stabilities.

Interatomic distances for **8/12A** are given in Figure 11. The small or nonexistent variations in geometry between charge states suggest a HOMO that is mostly nonbonding in character, and examination of the molecular orbital contours of the HOMO shows lobes based mainly on Nb^{o} and directed out of the molecule. The electronic structure of **8/12A** is discussed in further detail below.

The single isomer considered for 8/13 is C-centered **8/12A** (retaining symmetry T_d) which has been discussed for Ti and other metals.[50,51,58,86] Experimental evidence for a C-centered 8/13 structure has been reported on the basis of reactive losses.[46]

Nb_9C_8, Nb_9C_9, and Nb_9C_{10}. Optimized structures for 9/8, 9/9, and 9/10 are presented in Figure 12. The most stable structures for each of the three compositions are closely related, being dominated by the presence of C atoms rather than C_2 groups. **9/8A** and **9/10A** are based on the structure of **9/9A**, which has the connectivity of four fused cubane units, or two fused **6/6A** units, or a 2 × 3 × 3 nanocrystallite. **9/8A** is **9/9A** with the square-coordinated C atom removed, whereas **9/10A** involves the replacement of one C atom along an edge of the molecule with a C_2 group, forming a type-**1A** cradle. **9/8B** is a square antiprism of Nb atoms capped on one Nb_4 face with an extra Nb, which then accommodates four C_2 groups in the cradle configuration. **9/8C** is again a monocapped square antiprism, but with isolated C atoms capping 8 of the resulting 12 Nb_3 faces. **9/9B** and **9/10D** are generated from **9/8B** by capping the remaining Nb_4 face with a C atom and a C_2 unit, respectively. **9/10B** is **9/8A** with two C atoms replaced by C_2 units in cradle formation, **9/10C** is generated from this structure by a 90° rotation of the C_2 groups. **9/9C** is an extension of **6/6B** and consists of stacked Nb_3C_3 hexagons; in analogy to **6/6B**, the three fewer Nb−C bonds of **9/9C** in comparison to **9/9A** result in a net destabilization of 66 kcal mol^{-1}. **9/8B** and **9/9B** are most likely destabilized by the presence of undercoordinated Nb atoms resulting from increased C−C bonding. **9/8C** is related

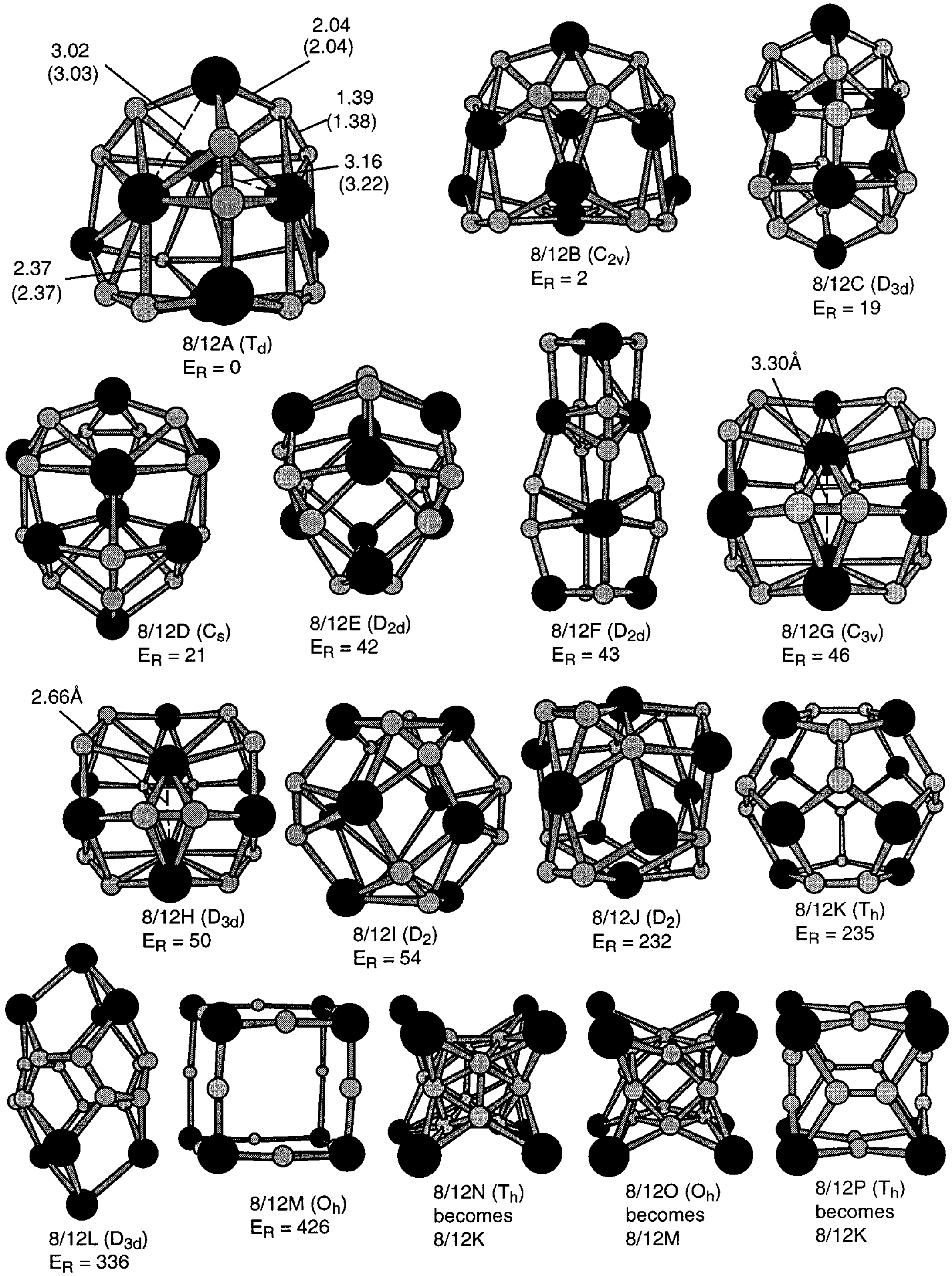

Figure 11. Optimized isomers of Nb_8C_{12}. Symbols as in Figure 2.

to **6/8E** and similarly demonstrates an unfavorability of μ_3-C atoms, which is believed to occur because these μ_3-Cs are too close together and repulsive but are unable to form C−C bonds because of symmetry constraints.

Notably, **9/8A** and **9/9A** are very much more stable than the alternatives. For **9/8A**, there is little structural variation between charge states, suggesting a nonbonding HOMO. However, there exists a wide range of Nb−C distances in this molecule, some of which are shown in Figure 12. **9/9A** is very similar in dimension to **9/8A**, and again the geometry changes little with a change in charge state. The inclusion of the extra C atom in **9/9A** introduces two new symmetry-independent Nb−C distances, radial and axial, which are marked in Figure 12. The axial Nb−C bond in the cation, with a length of 2.54 Å, is still quite long and is likely to be nonbonding, suggesting that the contraction of this distance with the loss of an electron is likely to be driven by the stereochemistry of the axial C atom rather than increased bonding. It is noted that the axial C atom is considerably out of the plane of the four Nb atoms surrounding it, and this deviation from planarity is sensitive to the charge state of the cluster.

In the 9/10 series, **9/10A** is derived from **9/9A** by a C $\Rightarrow$ C_2 substitution, in close analogy to the generation of **6/7A** from **6/6A**. The composition 9/11 is observed experimentally, but 9/12 is neither abundant nor identified, which supports the conclusion that one or two C $\Rightarrow$ C_2 substitutions in a nanocrystal fragment

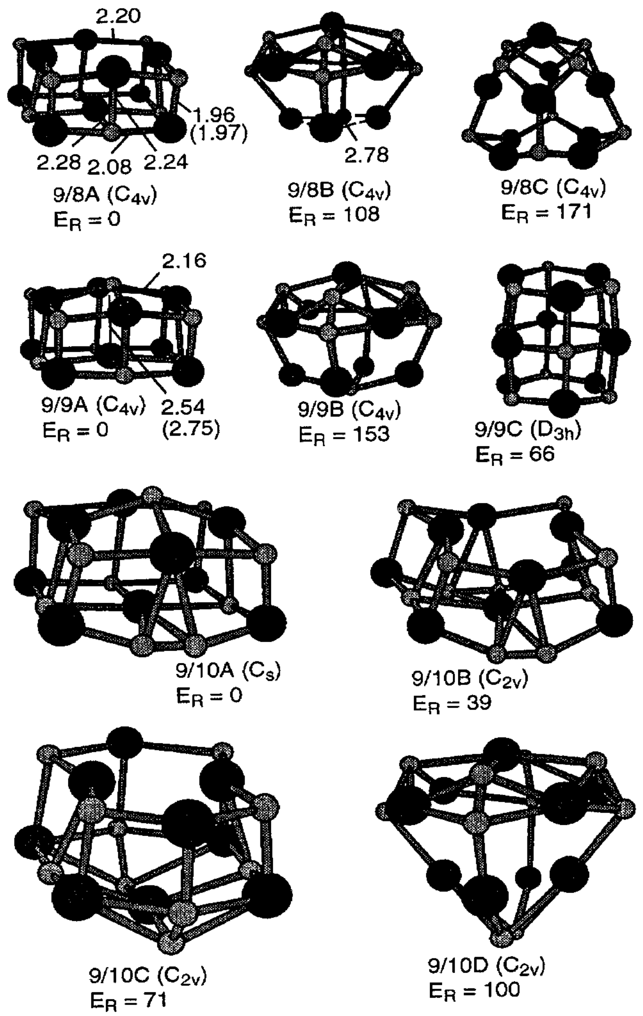

Figure 12. Optimized isomers of Nb_9C_8, Nb_9C_9, and Nb_9C_{10}. Symbols as in Figure 2. Selected distances (Å) are marked for the monocations; distances for the neutral are given in parentheses when they differ by more than 0.01 Å from those for the cation. **9/9B** and **9/9C** are labeled in reverse energetic order to maintain consistency with the **9/8** series.

of this size can be accommodated and are feasible, but no more. From Table 1, it is noted that **9/10A** has a slight advantage over **9/9A** in normalized binding energy and ionization energy, but 9/10 is not more abundant than 9/9.

$Nb_{10}C_{12}$. The six isomers optimized for 10/12 are shown in Figure 13. The first three are much more stable than the remainder. The most stable structure, **10/12A**, is a fusion of **9/8A** and a 4-fold spire; there are four C_2 groups in cradles that are close to planar (type **1B**) and four C atoms with 4-fold orthogonal stereochemistry. Structure **10/12B**, which is only marginally less stable than **10/12A**, is a fusion of **9/9C** and a 3-fold spire, possessing three C_2 groups and six isolated C atoms. **10/12C** is a fusion of **9/9C** and a 3-fold wheel and is related to **10/12B** by a 90° rotation of all C_2 units. An alternative view of the construction of **10/12B** and **10/12C** involves addition of a Nb_3C_3 base to **7/9A** and **7/9B**, respectively. The stability of **10/12B** and **10/12C** can be related to the stability of the smaller units that compose them.

The 4-fold spire, which appears for the first time in **10/12A**, has cradled C_2 groups with dimensions different from those of the 3-fold spire. Comparing the cradles in **8/12A** and **10/12A**, the $M^{\sigma}{-}C$ distance in **10/12A** increases from 2.04 to 2.38 Å, whereas the $M^{\pi}{-}C$ distances decrease from 2.37 to 2.20 Å. The increase in $M^{\sigma}{-}C$ is partly a consequence of the increased coordination number of the apical M^{σ} in **10/12A**.

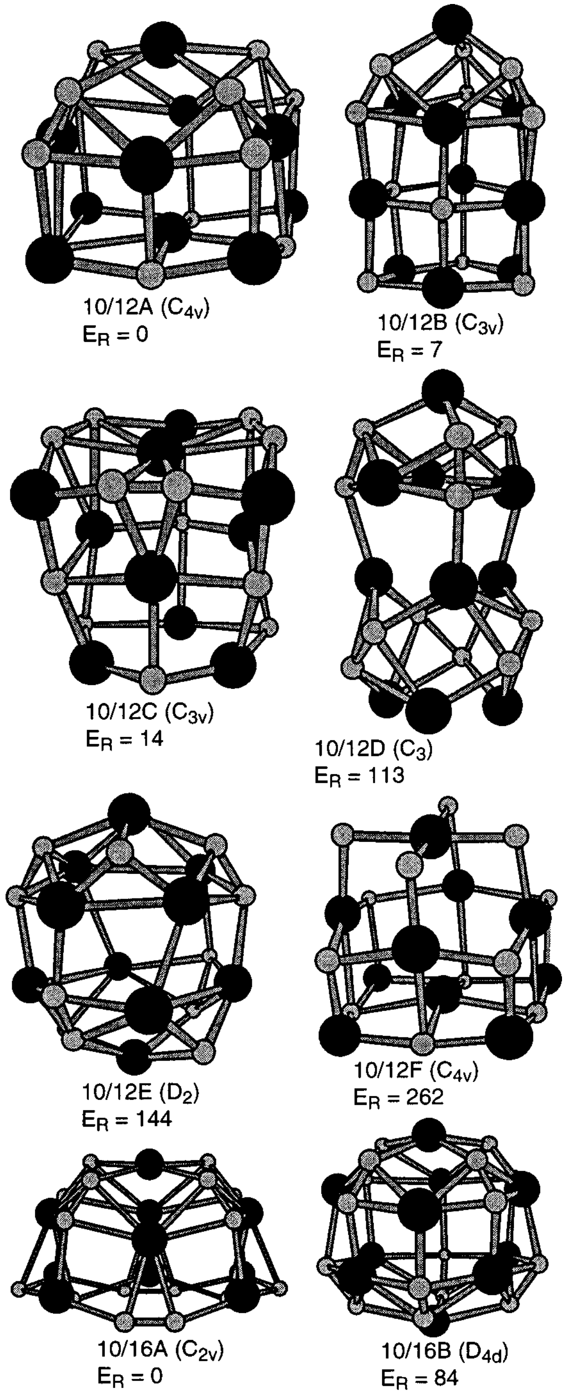

Figure 13. Optimized isomers of $Nb_{10}C_{12}$ and $Nb_{10}C_{16}$. Symbols as in Figure 2. The primary rotation axes of each structure are near vertical and near the plane of the page.

Structure **10/12D** could be regarded as **10/12B** with the lowest Nb_3C_3 hexagon rotated to form three more cradled C_2 units or as the fusion of **6/6C** and a 3-fold spire. The lesser stability of **10/12D** could thus be related to the lower stability of the features of **6/6C**. Isomer **10/12E** is an axially bicapped square antiprism of Nb atoms, with four C_2 groups cradled as type **1B** and four μ_3-C atoms. The low stability of **10/12E** can be attributed to the flattening of the trigonal coordination of the μ_3-C atoms, away from the more orthogonal coordination of C, caused by the 4-fold nature of the Nb polyhedron. The occurrence of uncapped Nb_3 faces in **10/12E** is presumably also a contributor to its lower stability. Structure **10/12F** is a depleted fragment of the cubic crystal lattice, with very low relative stability because of the two-coordinate C atoms.

The relative energies of the six 10/12 structures do not correlate with the relative numbers of C atoms or C_2 groups but demonstrate the importance of appropriate local coordination geometry and how the fusion of moieties can enhance or upset local coordination stereochemistry.

$Nb_{10}C_{16}$. Two structures were evaluated for 10/16 (see Figure 13). The more stable structure, **10/16A**, is generated from **10/12A** by four C $\Rightarrow$ C_2 replacements. A conceivable structure for 10/16 is a 4-fold spire bound to a 4-fold wheel, in the same way that **8/12A** is a 3-fold spire bound to a 3-fold wheel. However, a 4-fold wheel is not geometrically feasible, as the increased radius would lengthen the $Nb^{\pi}-C$ distance to a point where strong bonding is not possible. **10/16A** is as close to this ideal as possible, with a 4-fold spire bound to a $Nb_5(C_2)_4$ fragment that is part wheel and part spire. In the optimized structure, there is severe distortion of two of the cradles at the base of **10/16A**, which occurs because the axial Nb atom at the base has moved inside the cluster to 2.98 Å from the apical axial Nb atom, providing some Nb−Nb bonding stabilization. This is not present in **10/16B**, which is derived from **10/16A** by rotation of just two C_2 groups. Structure **10/16B** can also be derived from **10/12E** by converting all remaining C atoms to C_2 groups such that there are eight cradle formations surrounding a bicapped square antiprism of Nb atoms. Isomer **10/16B** can also be described as base-to-base fusion of two 4-fold spires.

The normalized binding energy of **10/16A**$^+$ [$BE''(+) = -31.1$ kcal mol^{-1} per valence electron, see below] is more negative than those of other nearby compositions and is comparable to the values for **8/12A** and **8/13A**, supporting the hypothesis that the occurrence of cradles, spires, and wheels confers stability. The slightly higher calculated ionization energy of **10/16A^0** (5.7 eV) over **8/12A^0** (5.3 eV) provides a partial explanation for its low observed abundance.

$Nb_{11}C_{13}$. Only one isomer, **11/13A**, was optimized, to the structure shown in Figure 14. It has C_{3v} symmetry and contains a central μ_4-C atom bonded to the hub Nb atom of a wheel moiety. **11/13A** can also be regarded as **10/12C** with a central C atom and an extra Nb atom capping the end Nb_3C_3 hexagonal face.

$Nb_{11}C_{15}$. Three structures were evaluated for the composition 11/15 (Figure 14). They are most readily understood as fusions of 3-fold spires and/or wheels to both sides of a Nb_3C_3 hexagon. The most stable structure **11/15A** is a pair of spires extending in both directions from the central Nb_3C_3 cycle, and ideally has D_{3h} symmetry. **11/15B**, also ideally D_{3h}, is similarly a pair of wheels fused to the central cycle, whereas **11/15C** has a spire on one side and a wheel on the other side of the Nb_3C_3 cycle and is ideally C_{3v}. There are analogies between these three 11/15 structures and the structures of **7/9A** and **7/9B**, which have a single spire or wheel fused to the Nb_3C_3 cycle. In effect, the **11/15A**,**B**,**C** isomers are double-ended versions of the single-ended **7/9A**,**B** structures. All three **11/15A**,**B**,**C** isomers exhibit distortion to lower symmetry, C_{2v} for **11/15A** and **11/15B** and C_s for **11/15C**, in a fashion similar to the symmetry reduction of **7/9A** and **7/9B**. This distortion is reflected in the Nb−Nb distances around the central belt of the molecules, which are as follows: for **11/15A^0**, two at 3.1 Å and one at 3.0 Å; for **11/15B**, two at 2.7 Å and one at 3.3 Å; and for **11/15C**, two at 3.0 Å and one at 3.2 Å. These three structures can also be thought of as **8/12C**, **8/12H**, and **8/12A**, respectively, extended by adding an equatorial Nb_3C_3 hexagon. All three of these isomers of 11/15 have favorable normalized binding energies (see below), which is consistent with the occurrence of the favorable spire and wheel moieties (however, see note in discussion regarding normalized binding energies of carbon-rich species).

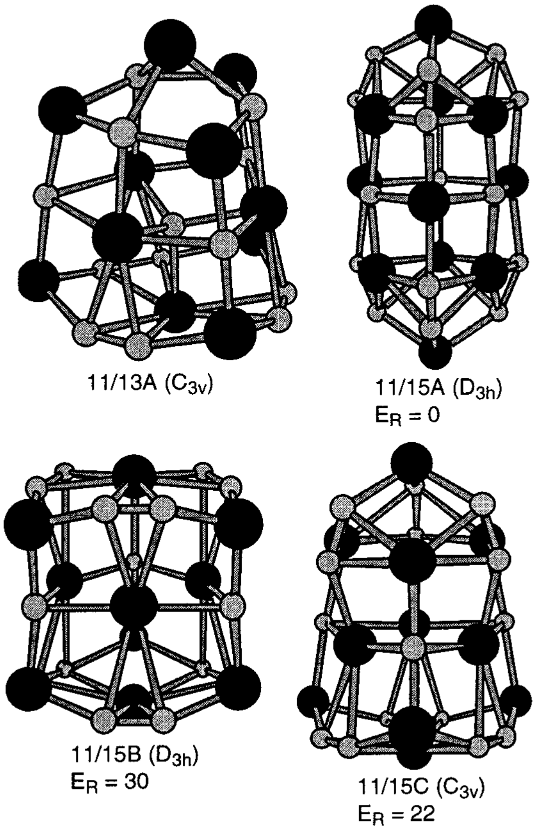

Figure 14. Optimized isomers of $Nb_{11}C_{13}$ and $Nb_{11}C_{15}$. Symbols as in Figure 2. The primary rotation axes of each structure are near vertical and lie within the plane of the page.

$Nb_{12}C_{12}$. The four isomers considered for 12/12 are pictured in Figure 15. **12/12A** is six fused cubanes, or the 2 × 3 × 4 nanocrystallite, whereas **12/12B** is an alternative fusion of six cubanoid units but with the central Nb atom removed. **12/12B** can be readily visualized as the 3 × 3 × 3 nanocrystallite with the central Nb atom and two diagonally opposite corner C atoms removed. Of these two structures, the more regular and orthogonal fragment, **12/12A**, is favored by 90 kcal mol^{-1} (in the neutral) or 100 kcal mol^{-1} (in the cation). **12/12C** is two fused **6/6B** molecules or six stacked Nb_3C_3 hexagons. Structure **12/12C** is a more open, pseudohexagonal form of **12/12A**, with fewer Nb−C bonds, resulting in destabilization relative to **12/12A** by more than 100 kcal mol^{-1}; this is analogous to the destabilization of **6/6B** relative to **6/6A** and of **9/9C** relative to **9/9A**. The high-symmetry (T_h) structure **12/12D** is based on a cuboctahedron of Nb atoms with C_2 groups on the quadrilateral faces. There is a distortion of the cuboctahedron toward an icosahedron, which shortens slightly the $M^{\pi}-M^{\pi}$ distances in the cradles, which are distorted slightly from type **1B** toward type **1C**. The lesser stability of **12/12D** (with C_2 groups) relative to **12/12A** (with C atoms) is probably a consequence of reduced or poor coordination of the Nb atoms. Indeed, capping two Nb_3 faces of **12/12D** to yield **12/14B** results in an improvement in the normalized binding energy.

The bond distances in **12/12A** are similar to those in **9/9A**, with the less-coordinated atoms at the extremes being more closely bound to neighbors than those with higher coordination. **12/12A** also shows the distortion seen for **9/9A**, where the square-coordinate carbon atoms are pushed out of the plane of

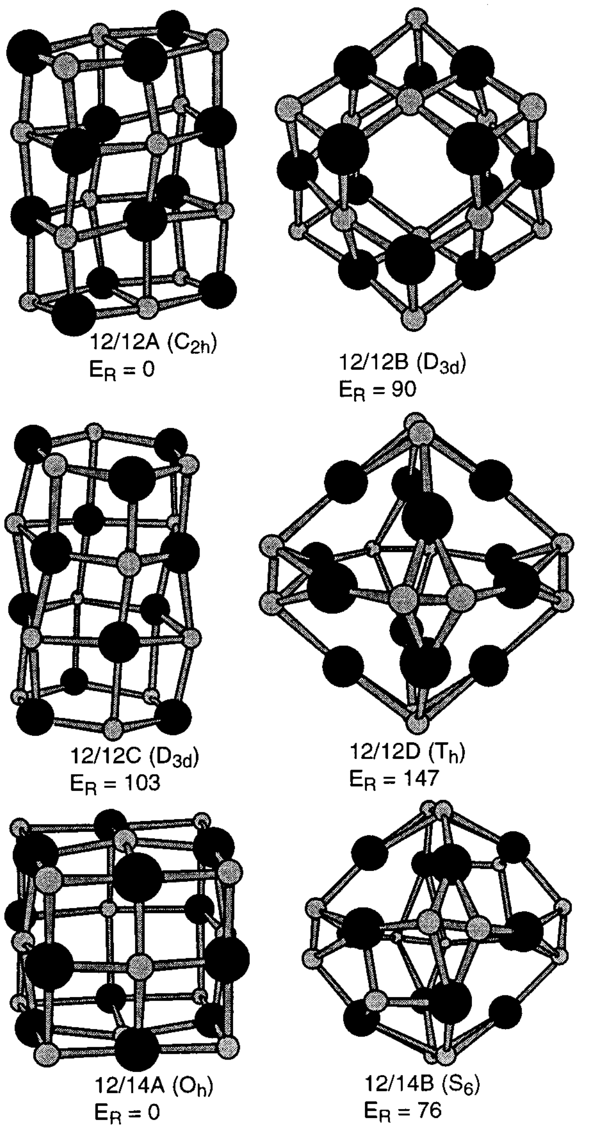

12/12A (C_{2h}) $E_R = 0$

12/12B (D_{3d}) $E_R = 90$

12/12C (D_{3d}) $E_R = 103$

12/12D (T_h) $E_R = 147$

12/14A (O_h) $E_R = 0$

12/14B (S_6) $E_R = 76$

Figure 15. Optimized isomers of $Nb_{12}C_{12}$ and $Nb_{12}C_{14}$. Symbols as in Figure 2. The primary rotation axes of each structure are near vertical and the plane of the page, except for **12/12A** and **12/12B**.

the four surrounding Nb atoms, and as in **9/9A,** this distortion is more than 0.2 Å larger in the neutral than in the cation.

$Nb_{12}C_{14}$. Two structures were evaluated for 12/14 (see Figure 15). The high-symmetry (O_h) isomer **12/14A** is a 3 × 3 × 3 nanocrystallite (i.e., **13/14A**) with the central Nb atom removed. This isomer is 76 kcal mol^{-1} more stable than **12/14B**, which is **12/12D** with two extra C atoms capping opposite Nb_3 faces. **12/14A** has a HOMO−LUMO gap of less than 0.03 eV, and many low-lying electronic states are accessible.

$Nb_{12}C_{15}$. The four structures evaluated for 12/15 are pictured in Figure 16. **12/15A** is derived from **11/15B** by the addition of a central Nb atom, but on optimization, the idealized D_{3h} symmetry is lost, and the central Nb atom forms a short bond to one of the three Nb atoms in the central Nb_3C_3 hexagon at a distance of 2.51 Å in the neutral and 2.45 Å in the cation. There is not enough room for the insertion of a central Nb atom in either **11/15A** or **11/15C**. Structure **12/15B**, which is **12/12D** augmented by capping C atoms on three Nb_3 faces, distorts from its ideal symmetry of C_3 to C_1. Structure **12/15C** differs from the others considered so far in that it has no C_2 groups but rather two C_3 groups and nine C atoms (five μ_4, four μ_3), and its energy indicates that these are not stabilizing features.

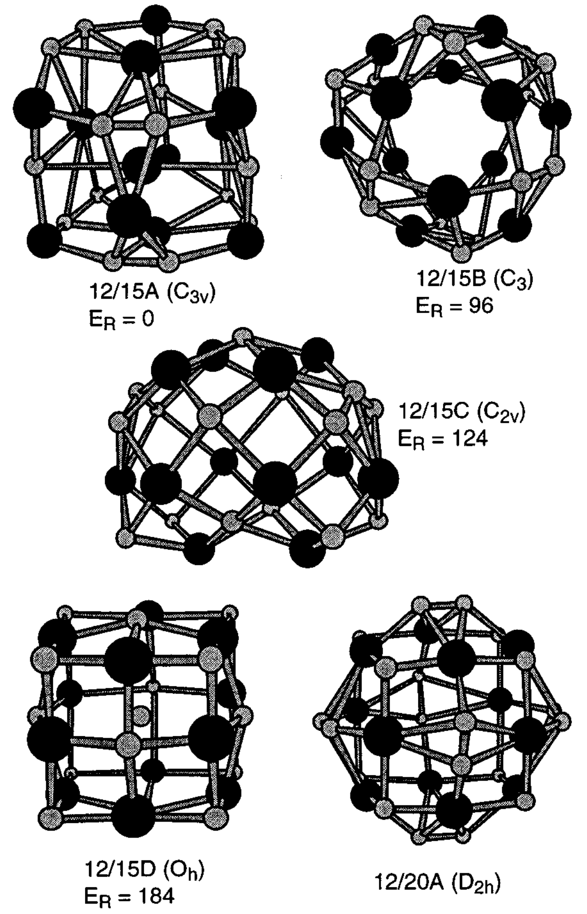

12/15A (C_{3v}) $E_R = 0$

12/15B (C_3) $E_R = 96$

12/15C (C_{2v}) $E_R = 124$

12/15D (O_h) $E_R = 184$

12/20A (D_{2h})

Figure 16. Optimized isomers of $Nb_{12}C_{15}$ and $Nb_{12}C_{20}$. Symbols as in Figure 2. The 3-fold axis of **12/15B** is perpendicular to the plane of the page, whereas all other structures have their primary rotation axes near vertical and in the plane of the page.

Structure **12/15D** with idealized O_h symmetry is C-centered **12/14A**, but it is better seen as the 3 × 3 × 3 nanocrystallite with the central Nb replaced by C, which is clearly an unfavorable feature because the central C atom is unbound.

The relative stability of **12/15A** is presumed to be due to the occurrence of two wheel units and a suitable mix of C atoms and C_2 groups. **12/15B** is of somewhat lower stability, most likely because of the poorer geometry of the Nb_4C_2 cradles in that the $M^{\pi}-C-M^{\pi}$ angles are greater than in **12/15A** (type **1B** versus **1A**).

$Nb_{12}C_{20}$. $[Nb_{12}C_{20}]^+$ is not observed with significant abundance (see Figure 1), but one isomer, **12/20A**, is calculated as an extension of the structure type introduced with **12/12D**. **12/20A** (see Figure 16) has the high symmetry T_h and is generated by the μ_3-C capping of all eight Nb_3 faces of **12/12D**. The electron-normalized binding energy for **12/20A** is not competitive, which can be attributed to the distortion of the six type-**1B** cradles in which the $M^{\pi}-C_2-M^{\pi}$ angles are too large. The ionization energy of **12/20A** is relatively high.

$Nb_{13}C_{14}$, $Nb_{14}C_{12}$, $Nb_{14}C_{13}$, $Nb_{14}C_{14}$, $Nb_{14}C_{15}$, and $Nb_{14}C_{16}$. The 3 × 3 × 3 nanocrystallite allows two compositions, 14/13 and 13/14, related by interchange of Nb and C atoms. The optimized structures for these species are pictured in Figure 17 as **14/13A** and **13/14A**. The **14/13A** structure is regarded as the "normal" 3 × 3 × 3 nanocrystallite and **13/14A** as the "inverse" 3 × 3 × 3 nanocrystallite for the reason that **$14/13^+$** is abundant in the experimental distribution, whereas **$13/14^+$** is essentially nonexistent (this is also true for other metals). Even though the total number of bonds is the same in the two

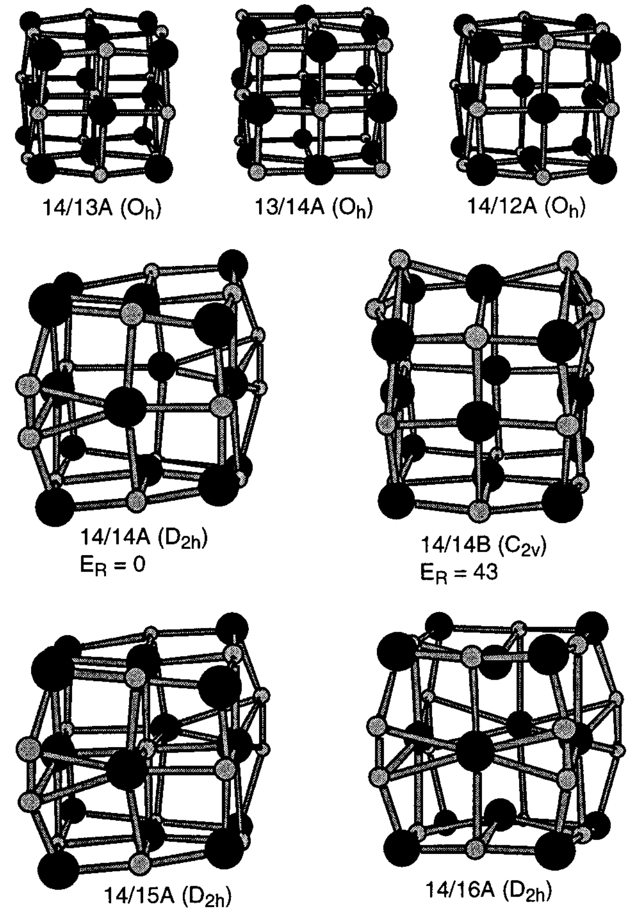

Figure 17. Optimized isomers of $Nb_{14}C_{13}$, $Nb_{13}C_{14}$, $Nb_{14}C_{12}$, $Nb_{14}C_{14}$, $Nb_{14}C_{15}$, and $Nb_{14}C_{16}$. Interatomic distances in **14/13A⁰** (**14/13A⁺**) are as follows: $Nb^{facial}-C = 2.31$ Å (2.30 Å), $Nb^{apical}-C = 2.13$ Å (2.12 Å), $Nb^{facial}-C^{central} = 2.13$ Å (2.13 Å), $Nb^{facial}-Nb^{apical} = 2.98$ Å (2.98 Å), and $Nb^{facial}-Nb^{facial} = 3.00$ Å (3.02 Å).

structures, the local stereochemistries are different, with the normal structure **14/13A** possessing 1 octahedral C atom and 12 four-coordinate C atoms, whereas **13/14A** has 8 trigonal-orthogonal C atoms and six square-pyramidal C atoms. Because it is likely that the bonding requirements of carbon are less flexible than those of niobium and because valence bond concepts allow 2sp + 2p hybridization for the four-coordinate C atoms in **14/13A**, this normal nanocrystallite structure would be expected to be more stable. The normalized binding energies (see Figure 18) for the neutral clusters show only a modest advantage of **14/13A^0** over **13/14A^0** but a larger advantage for the cations, consistent with the experimental data in which 14/13 is considerably more abundant than 13/14. The significant result of the DF calculations is that the ionization energy of **13/14A**, 5.6 eV, is much larger than those of **14/13A**, 3.9 eV, and other clusters of similar size, and so the poor abundance of **13/14$^+$** is attributed to the excessive ionization energy of its most symmetrical isomer.

Structure **14/12A** is **14/13A** without the central μ_6-C atom, and it has similarly favorable normalized binding energies and ionization energy. The composition 14/14 is generated from **14/12A** by two C ⇒ C_2 substitutions. Two of the many ways in which the C_2 groups can be positioned are shown as **14/14A** and **14/14B**, with an energy advantage for the trans isomer **14/14A** in which the C_2 groups are not bound to the same Nb atom. There is a large difference in the calculated ionization energies of these two isomers, with **14/14A** having an IE (3.9 eV) that is similar to those of other clusters of this size but with **14/14B** having an unusually large ionization energy of 6.3 eV.

The compositions 14/15 and 14/16 can be modeled by C ⇒ C_2 substitutions in the preceding structures, without or with the central μ_6-C atom, respectively, and two such symmetrical isomers are shown in Figure 17 as **14/15A** and **14/16A**. Both have competitive normalized binding energies. It is significant that all of the most stable isomers for the $Nb_{14}C_y$ clusters have calculated ionization energies between 3.9 and 4.0 eV and that such low ionization energies are not calculated for compositions with fewer atoms.

Absolute Stabilities. To compare stabilities of different compositions we have calculated normalized binding energies. Figure 18 shows the normalized binding energies per atom (BE′) for the most stable isomer of each composition, plotted versus the cluster mass for both the neutral and cationic clusters. Also shown is a similar plot of the normalized binding energies per valence electron (BE″), with the assumption that, in general, four C electrons and five Nb electrons will contribute principally to the bonding. BE″ is intended to take better account of the range between C-deficient and C-rich clusters. All four plots show the same general pattern, which will be discussed below in the context of the formation and observed distributions of Nb_xC_y clusters. We note that the similarity between the plots (Figure 18) for the different charge states reinforces the general conclusion that the electrons at the Fermi level in these compounds are not strongly bonding or antibonding.

Discussion

This discussion reflects the questions raised in the Introduction: What are the geometrical structures and structural principles for the Nb_xC_y clusters? What are the bonding principles? Which properties account for the distributions and reactivities of the observed ions? We then consider distortions in the nanocrystallite structures and the implications of our results for the photodissociation of $[Nb_{14}C_{13}]^+$ and for met−cars with other metals.

Geometric Structure Types and Principles. Readily categorized structure types and substructures are recognized. We consider first those with only C atoms and no C−C bonds.

(a) Symmetrical Fragments of the Cubic NbC Lattice. The compositions 4/4, 6/6, 9/9, 12/12, and 14/13 are most stable (in isomers **4/4A**, **6/6A**, **9/9A**, **12/12A**, and **14/13A**) as symmetrical fragments of the cubic NbC lattice.

(b) Stacked Nb_3C_3 Hexagons. Intersecting set a is a related set consisting of stacked Nb_3C_3 hexagons, namely, **6/6B**, **9/9C**, and **12/12C**; **3/3F** is the single hexagon. This stacked-hexagon structure type has been established as stable for these compositions of manganese sulfide clusters Mn_xS_y.[75] Key distinctions between sets a and b are the orthogonality of local coordination stereochemistry at C and the absence of some transannular Nb−C bonds in the stacked-hexagon type b. Our results show conclusively that the more favorable of these two structural types is the regular fragment of the cubic lattice a.

(c) Substructural Fragments of the Cubic NbC Lattice. The small structures **2/2A**, **3/3A**, **3/4A**, and **4/3A** are less regular fragments of the cubic lattice but are relatively stable. A comparison of **3/3A** and **3/3E**, which have the same connectivity and are both lattice fragments, shows that the tri-orthogonal coordination of C in **3/3A** is preferable. The isomer **5/6A** is a fusion of two cubanes. The isomers **9/8A** and **9/10A** are minor modifications of **9/9A** and largely consist of the cubic NbC lattice, as does **10/12A**. Whereas these results indicate the stability of the cubic lattice, less symmetrical or more exten-

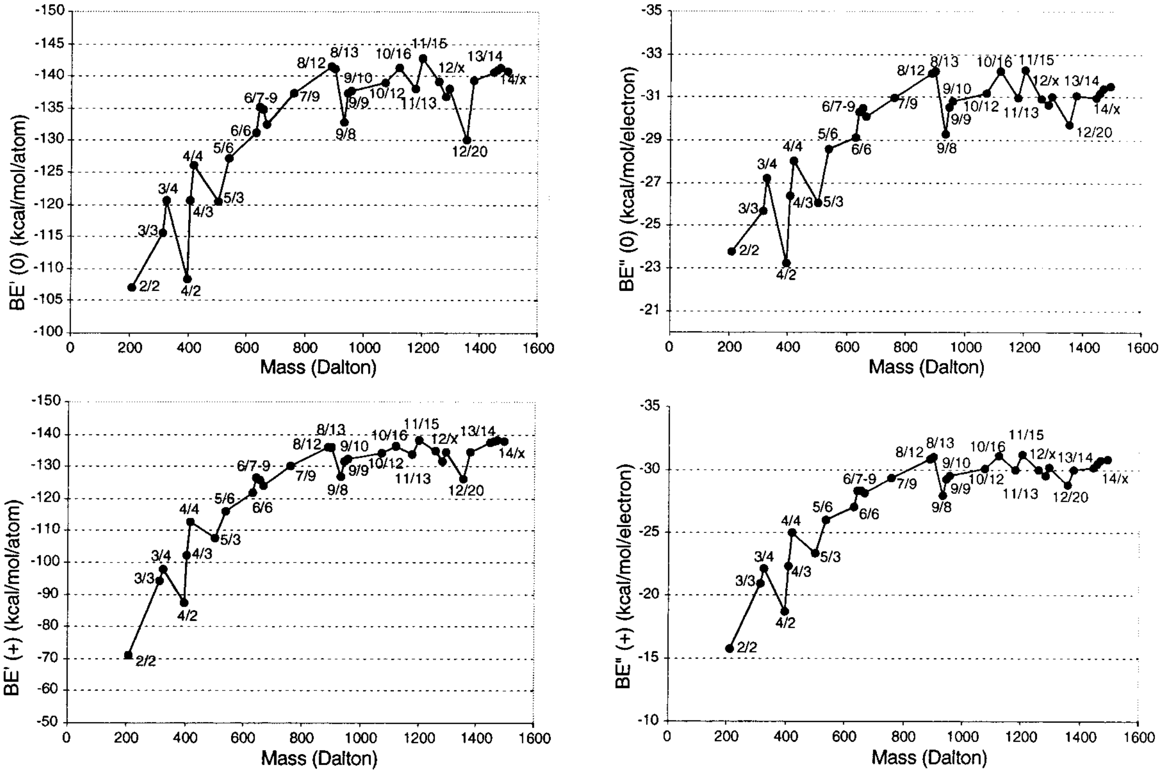

Figure 18. Plot of the normalized binding energies per atom (BE′) and per valence electron (BE″) versus cluster mass for the neutrals (top) and cations (bottom) of the most stable isomer found for each of the experimentally observed compositions.

sively voided fragments of the cubic lattice (**4/4C**, **7/9C**, **10/12F**) are very much less stable than alternative structures. Isomer **12/15D** shows that substitution of C for Nb with concomitant overcoordination of C with other C atoms is quite unfavorable.

We now consider involvement of C_2 groups.

(d) Structures Containing Only C_2 Groups. These are **2/2B**, **4/2B**, **4/4B**, **4/4D**, **5/6B**, **6/6C**, **6/6D**, **6/8D**, **8/12A**, **8/12B**, **8/12C**, **8/12D**, **8/12E**, **8/12G**, **8/12H**, **8/12I**, **8/12K**, **8/12P**, **9/8B**, **9/10D**, **10/12D**, **10/16A**, **10/16B**, and **12/12D**. Of these, only two C-rich compositions, 8/12 and 10/16, have C_2-only isomers as the most stable, namely, **8/12A** (and **8/12B**, which is very similar in energy to **8/12A**) and **10/16A**. This reinforces the general conclusion that can be drawn simply from the ion map (Figure 1) for $[Nb_xC_y]^+$ clusters, that *y*-odd and C-atom structures are common.

(e) Longer Carbon Chains. Carbon chains C_3 or C_4, or carbon cycles, are not stable in the Nb_xC_y clusters. Structures **6/7D**, **8/12J**, **8/12L**, **8/12D**, and **12/15C** demonstrate this conclusion.

(f) C ⇒ C_2 Substitution. For Nb_xC_y clusters with $y > x$, energetically favorable structures are commonly related to $y \approx x$ isomers by substitution of C atoms with C_2 groups. The smallest example of this is seen for **6/7A**, where a C atom on the long edge of **6/6A** is replaced, resulting in a structure with a single type-**1A** cradle. Other instances of this C ⇒ C_2 substitution generate **6/7B**, **6/7C**, **6/8B**, **8/12D**, **9/10A**, **9/10B**, **9/10C**, **14/14A**, **14/14B**, **14/15A**, and **14/16A**, including many of the most stable isomers.

(g) Spire and Wheel Substructures. The placement of C_2 groups in the cluster structures is favorable when they generate the 3-fold spire or wheel moieties (Figure 9). This is evident in the isomers **7/9A**, **7/9B**, **8/12A**, **8/12B**, **8/12C**, **10/12A**, **10/12B**, **10/12C**, **11/13A**, **11/15A**, **11/15B**, **11/15C**, and **12/15A**, which include the most stable isomers for these compositions. The spire and the wheel of Figure 9 are regarded as the key substructures to be incorporated in the postulation of structures for met−cars.

(h) Fusion of Spires or Wheels with C-Atom Sections. Larger structures for Nb_xC_y can successfully fuse a 3-fold spire or 3-fold wheel (or both) containing C_2 groups with a section that contains isolated C atoms. Because the C-atom structures are more stable when orthogonal rather than 3-fold or hexagonal, there is a conflict between the geometrical requirements of the two fused substructures. This occurs in **7/9A**, **7/9B**, **10/12B**, **10/12C**, **11/15A**, **11/15B**, and **11/15C**. In general, the optimizations of these structures have caused the C-atom section of the cluster to comply with the 3-fold geometry of the C_2 section, which indicates the greater stabilization achieved by regular spire and wheel substructures.

(i) Nb_4C_2 Cradle. The Nb_4C_2 cradle is another important substructure for met−cars with C_2 groups (Figure 9). The general conclusion is that, although there is considerable variability in the geometry of the cradle, the general order of stability by cradle type is **1A** > **1B** > **1C**. This is borne out by results for the structures **11/15A** and **11/15B**, among others.

Finally in this discussion of geometric structure, we comment that there are other untested lower-symmetry structures, particularly for the larger clusters. Our conclusions have been drawn from the large but limited number (100) of structures calculated. However, the process of generating structures was expert in the sense that the principles of local coordination from small structures, and the evolving favorable substructures, were incorporated in postulated structures of the larger clusters.

Which Properties Account for the Observed Distributions? The accumulated results in Table 1, and the recognition of structural principles, allow some response on the question raised in the Introduction about the factors which influence the observed patterns of $[Nb_xC_y]^+$ ions. The three main factors

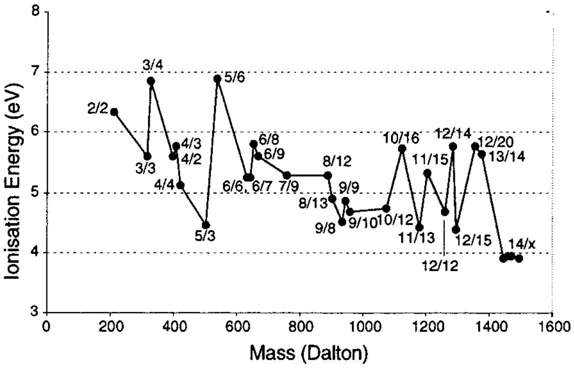

Figure 19. Plot of the calculated vertical ionization energies (eV) versus cluster mass for the most stable isomer found for each of the experimentally observed compositions.

considered as most influential on the observed distributions of $[Nb_xC_y]^+$ clusters are (i) thermodynamic stability; (ii) the competition for electrons in the plasma, such that species with high ionization energies are likely to exist as (unobserved) neutral clusters in the presence of observed species with lower ionization energies; and (iii) kinetic and entropic limitations.

Thermodynamic stabilities are compared through normalized binding (internal) energies (Figure 18). The ionization energies for the most stable isomer of each composition are plotted in Figure 19. A general pattern evident in the ionization energies is that clusters that are C-rich, i.e., have $y > x$, have higher ionization energies; some of the lower ionization energies are for Nb-rich clusters. Pronounced differences between the IEs for **5/3A** and **5/6A**, **10/12A** and **10/16A**, and **12/15A** and **12/20A** illustrate this generalization, but exceptions also occur (Figure 19). We suggest that the limitation on formation of more C-rich $[Nb_xC_y]^+$ clusters could be the uncompetitive ionization energies of the corresponding neutrals.

A general result is that the normalized binding energies are low for the smaller clusters 2/2, 3/3, 3/4, 4/2 and 4/3, particularly for the cations. The unavoidable undercoordination in these clusters is responsible for their low normalized binding energies. In addition, these smaller clusters have above-average ionization energies (see Figure 19), and these two properties are probably the reason for the low-mass limits of the ion map. The kinetics of formation of these small clusters should not be limiting.

The cubane cluster **4/4A** with favorable coordination shows local maxima in BE′ and BE″ for both neutral and cation, as well as a relatively low IE, consistent with its abundance in the mass spectra. Cluster **5/3A** has a competitive BE and a very favorable IE, whereas **5/6A** is probably observed because of its BE. The abundance of the compositions 6/7 and 7/9 is distinctive to Nb among M_xC_y systems, and this observation can be understood from the relatively high BE and low IE values calculated for **6/7A** and **7/9A**. Comparative data for these compositions in other metal systems will be useful.

From 8/12 to higher masses, normalized binding energies of the cations (both BE′ and BE″) are roughly constant, with notable excursions above (**8/12A**, **8/13A**, **10/16A**, **11/15A**, and **14/xA**) and below (**11/13A**, **12/13A**, and **12/20A**) the norm. Of the species with above-average binding energies, those with low or average ionization potentials (**8/12A**, **8/13A**, **11/15A**, and **14/xA**) tend to show high relative abundances in the mass spectrum. A locally high IE for **8/12A** might be the reason for the variations in abundance of 8/12 with experimental conditions. The low IEs of **11/13A** and **12/15A** are probable contributors to their experimental abundance, whereas **10/16A**, **12/14A**, **12/20A**, and the inverse 3 × 3 × 3 nanocrystallite **13/14A** all have high ionization potentials explaining their low relative abundances.

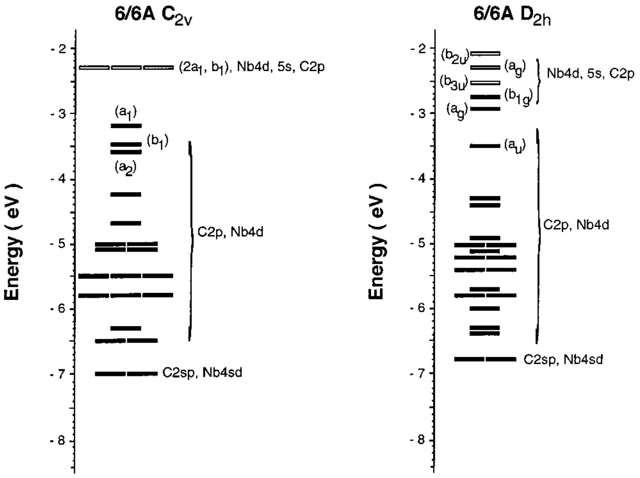

Figure 20. Calculated electronic structures of $\mathbf{6/6A^+}$ as calculated within the C_{2v} and D_{2h} point groups. Significant atomic orbital contributions to molecular orbitals are shown to the right of each MO. Filled rectangles represent occupied orbitals, open rectangles represent unoccupied orbitals. Symmetries of selected orbitals are given.

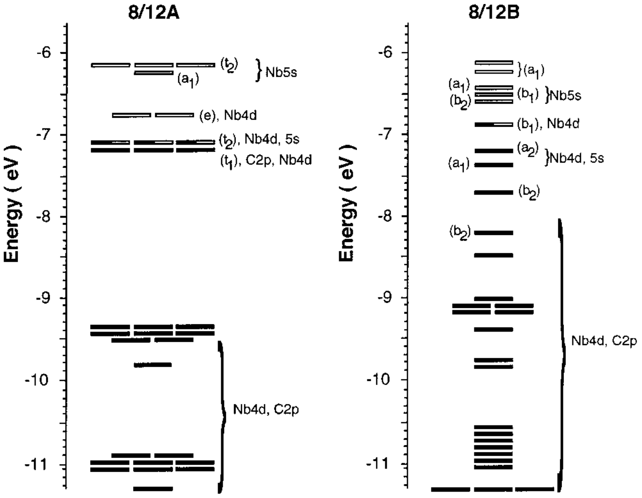

Figure 21. Calculated electronic structures of $\mathbf{8/12F^+}$ and $\mathbf{8/12H^+}$. Filled rectangles represent occupied orbitals, open rectangles represent unoccupied orbitals, and half-filled rectangles indicate partially occupied orbitals.

Figures 18 and 19 show that the stabilities increase and the ionization energies decrease with increasing mass, and that these two properties are favorable in the upper mass range. The diminishing abundance at high mass must be due to kinetic rather than thermodynamic factors.

Principles of Electronic Structure and Reactivity. Diagrams of the energies and compositions of frontier molecular orbital are presented for $\mathbf{4/4A^0}$ (Figure 5), $\mathbf{6/6A^0}$ (Figure 20), $\mathbf{6/7A^0}$ (Figure 5), and $\mathbf{8/12A^+}$ and $\mathbf{8/12B^+}$ (Figure 21). The general MO pattern for the neutral clusters is as follows (with the orbitals for the cations shifted to more negative energy): Below the orbitals included in the figures lie the Nb 4s atomic orbitals at ca −55 eV, the Nb 4p orbitals at ca. −35 eV, and the C 2s orbitals (between −11 and −13 eV in structures without C−C bonds or below −15 eV and above −10 eV with C−C bonds). As shown in Figures 5, 20, and 21, the Nb 4d and C 2p atomic orbitals combine to form a large number of bonding MOs in the vicinity of −10 to −5 eV, distributed according to the symmetry and size of the cluster. Further above this in the

HOMO−LUMO region are MOs composed mainly of Nb 4d and Nb 5s atomic orbitals. These are either weakly Nb−Nb bonding interactions or more commonly nonbonding MOs with outward pointing lobes based on Nb.

The ground-state electronic structure of **4/4A** has a doubly degenerate *e*-symmetry HOMO and a triply degenerate t_2 LUMO lying only 0.3 eV above the HOMO in the neutral and in the cation. The small HOMO−LUMO gap and the partially occupied HOMO of the cation suggest significant reactivity, which, in fact, is observed. It is reported that $Nb_4C_4^+$ reacts with oxygen to form $Nb_4C_2^+$ (and presumably CO_2) and that it reacts with water and alcohols, adding four ligands sequentially with concurrent loss of some H_2.[47]

Freiser et al. have also reported reactions of $[Nb_6C_7]^+$ with water, alcohols, ammonia, acetonitrile, and benzene.[22] The general pattern is efficient addition of four ligands, with limited addition of fifth and sixth ligands. This is entirely consistent with our structure **6/7A**, which contains four Nb atoms with only trigonal three-coordination and two Nb atoms with four-coordination ($3C + C_2$). Facile addition occurs at the under-coordinated Nb atoms and then reluctant addition at the more-coordinated Nb atoms (with assumed integrity of the $[Nb_6C_7]^+$ core). The only case where dehydrogenation was observed in reactions with $[Nb_6C_7]^+$ was with the addition of the fifth and sixth molecules of water to yield $[Nb_6C_7(H_2O)_5O]^+$ (or $[Nb_6C_7(H_2O)_4(OH)_2]^+$). The lower reactivity (in terms of both speed of reaction and extent of dehydrogenation) of $[Nb_6C_7]^+$ in comparison with $[Nb_4C_4]^+$ is interpreted as being due to the larger HOMO−LUMO gap and smaller number of close-lying excited states of **6/7A**.

Castleman and co-workers[43] have suggested that the number of unpaired electrons in these met−car species can be measured as the number of iodine atoms they add on reaction with methyl iodide. Freiser and co-workers report that both $[Nb_6C_7]^+$ [22] and $[Nb_4C_4]^+$ [47] add only one iodine atom, which is consistent with our calculated electronic structures (see Figure 5) in which **4/4A**$^+$ and **6/7A**$^+$ have one unpaired electron each. $[Nb_4C_4]^+$ reacts further with methyl iodide via dehydrogenation followed by addition to form $[Nb_4C_4I(CHI)(CH_3I)_{0-2}]$, whereas $[Nb_6C_7]^+$ shows no further reactions with CH_3I after the first iodine abstraction. Freiser suggests that this indicates that $[Nb_4C_4]^+$ has three nonbonding electrons, on the assumption that I and CHI bond with one and two electrons, respectively. This is consistent with our calculated electronic structures, which predict that $[Nb_4C_4]^+$ is more reactive than $[Nb_6C_7]^+$ and that $[Nb_4C_4]^+$ has three nonbonding electrons.

Figure 21 shows the calculated electronic structures for **8/12A**$^+$ and **8/12B**$^+$, which are calculated to be very similar in total energy. The high symmetry of **8/12A** and lower symmetry of **8/12B** are evident in the orbital dispersion, and in **8/12A**$^+$ there is characteristic gap of 2 eV below the close-lying HOMO and NHOMO. **8/12A**$^+$ is predicted to be a spin quartet, and **8/12B**$^+$ a spin doublet. The principal data through which **8/12A**$^+$ and **8/12B**$^+$ could be differentiated are the reactivity data. Freiser and co-workers report that $[Nb_8C_{12}]^+$ reacts with methyl iodide and abstracts five iodine atoms and that $[Nb_8C_{12}]^+$ reacts with water, alcohols, acetonitrile, ammonia, and benzene via stepwise addition, which is truncated after the addition of four ligands.[20] Assuming the Castleman hypothesis relating the number of unpaired electrons to the number of added iodine atoms, structure **8/12A**$^+$ is closer to the observation, as there are three unpaired electrons in the ground state and another close-lying t_1 orbital that could contribute unpaired electrons after the first abstractions of iodine atoms. The weakness in this interpretation is that the iodinated intermediates are likely to undergo geometrical and electronic rearrangement, but in the absence of calculations on such intermediates, it seems that **8/12A** is the more probable structure. This is also consistent with the addition of four Lewis base ligands, which would coordinate at the four outer Nb atoms of **8/12A**.

Distortion of Nanocrystallite Structures. Significant distortions are noted for **6/6A** and **9/9A**. This involves differentiation of the C atoms on the 2-fold axis of the molecule for the **6/6A** structure and a similar outward displacement of the μ_4-C atom on the 4-fold axis of **9/9A**. Figure 20 shows the calculated electronic structures for **6/6A^0** in the more stable lower-symmetry C_{2v} isomer (detailed in Figure 8), in comparison with the constrained D_{2h} structure. In the C_{2v} structure, there is general lowering of the orbital energies, and the three highest occupied MOs are reduced by an amount (0.5 eV) roughly equivalent to the total energy advantage of the C_{2v} structure. Further, there is a significantly higher contribution of C 2p orbitals to the MO of *b* symmetry, which is stabilized most in the C_{2v} structure. It seems that the relaxation in symmetry allows for an increased bonding interaction between Nb 4d and C 2p atomic orbitals that was unavailable in the D_{2h} structure. Similar distortions are noted for **7/9A**, **7/9B**, and **11/15C** (C_{3v} to C_s), as well as **11/15A** and **11/15B** (D_{3h} to C_{2v}), which are nanocrystallites altered by $C \Rightarrow C_2$ substitution. However, the reason behind these distortions remains unclear.

Photodissociation of $Nb_{14}C_{13}^+$. The observed photodissociation of $[M_{14}C_{13}]^+$ (M = Ti, V, and Zr) involves the sequential loss of M atoms, resulting in the dominant products with compositions 8/12 and 8/13, or the loss of MC or MC_2 moieties, resulting in less abundant product species such as 9/9.[15] In comparison, the photodissociation of $[Nb_{14}C_{13}]^+$ does not result in significant amounts of 8/13, 8/12 or 9/9 but mostly 6/7 and 4/4 products.[30] The absence of the 8/12, 8/13, and 9/9 compositions in the photodissociation spectrum of $[Nb_{14}C_{13}]^+$ could be because (1) these compositions are not produced, or (2) they are produced, but have higher ionization energies than the smaller fragments, and hence are not observed as positive ions. The results show a general downward trend in ionization energy as cluster size increases, which discredits the second possibility. If, then, the first situation is the case, i.e., the dissociative mechanism for $[Nb_{14}C_{13}]^+$ does not produce the 8/12, 8/13, and 9/9 compositions, even as neutrals, then the fragmentation observed in this system is far more extensive than that observed for $[M_{14}C_{13}]^+$ with Ti, V, and Zr. One interpretation of this result is that the 8/12, 8/13, and 9/9 compositions are not as stable for the niobium−carbon system as are the smaller compositions; however, this is opposite to the calculated trend in normalized binding energies (Figure 18). An alternative possibility is that the preferred dissociation mechanism for $[Nb_xC_y]^+$ clusters involves loss of large Nb_xC_y fragments and does not allow the formation of the 8/12, 8/13, or 9/9 compositions.

In conclusion, we believe that our calculations and interpretations generate a broad picture of the structures and properties of the observed Nb_xC_y clusters and provide specific structures. The reactivity patterns can be explained (although the photodissociation of $[Nb_{14}C_{13}]^+$ remains uncertain). Most importantly, the structural principles and the key substructural components have been defined. At the local level, Nb−C bonding is the principal source of stability, with Nb−Nb bonding energy less important but still significant. Cradle-motif Nb_4C_2 moieties are important, but not if they are strongly distorted. The 3-fold wheel substructure and the spire (3-fold or 4-fold) are key substructures involving C_2. Fused cubanoid units, such as occur in the nanocrystallites, are the main containers of C atoms and are usually slightly distorted. Substitution of C_2 in place of C in a nanocrystallite occurs in some Nb_xC_y clusters that are slightly C-rich. Fusion of wheels or spires onto nanocrystallite sections occurs with increasing C content, and the most C-rich clusters contain C_2 units only, but not longer C_n chains.

We expect that these structural principles will be broadly applicable to other M_xC_y clusters.

Acknowledgment. This research is supported by the Australian Research Council and the University of New South Wales. Hugh Harris acknowledges an Australian Postgraduate Award.

Supporting Information Available: Tables of Cartesian coordinates for each of the optimized structures, as the neutral molecule and as the monocation, and tables of some calculated vibrational frequencies. This material is available free of charge via the Internet at http://pubs.acs.org.

References and Notes

(1) Shelimov, K. B.; Clemmer, D. E.; Jarrold, M. F. *J. Phys. Chem.* **1994**, *98*, 12819−12821.

(2) Bartl, A.; Dunsch, L.; Fröhner, J.; Kirbach, U. *Chem. Phys. Lett.* **1994**, *229*, 115−121.

(3) Bethune, D. S.; Kiang, C. H.; Beyers, R.; van Lossdrecht, P. H. M.; de Vries, M. S.; Salem, J. R.; Yannoni, C. S.; Johnson, R. D.; Burbank, P.; Haynes, J.; Glass, T.; Stevenson, S.; Dorn, H. C. *Proc. IWEPNM94*, March 5−12, 1994, Kirchberg/Tirol, Austria; American Institute of Physics: Woodbury, NY, 1994.

(4) Clemmer, D. E.; Hunter, J. M.; Shelimov, K. B.; Jarrold, M. F. *Nature* **1994**, *372*, 248−250.

(5) Clemmer, D. E.; Shelimov, K. B.; Jarrold, M. F. *Nature* **1994**, *367*, 718−720.

(6) Shelimov, K. B.; Jarrold, M. F. *J. Am. Chem. Soc.* **1995**, *117*, 6404−6405.

(7) Suzuki, S.; Torisu, H.; Kubota, H.; Wakabayashi, T.; Shiromaru, H.; Achiba, Y. *Int. J. Mass Spectrosc. Ion Processes* **1994**, *138*, 297−306.

(8) Shinohara, H. *Rep. Prog. Phys.* **2000**, *63*, 843−892.

(9) Wei, S.; Guo, B. C.; Purnell, J.; Buzza, S.; Castleman, A. W. *J. Phys. Chem.* **1992**, *96*, 4166−4168.

(10) Wei, S.; Guo, B. C.; Purnell, J.; Buzza, S.; Castleman, A. W. *Science* **1992**, *256*, 818−820.

(11) Guo, B. C.; Kerns, K. P.; Castleman, A. W. *Science* **1992**, *255*, 1411−1413.

(12) Yamada, Y.; Castleman, A. W. *Chem. Phys. Lett.* **1993**, *204*, 133−138.

(13) Guo, B. C.; Wei, S.; Chen, Z.; Kerns, K. P.; Purnell, J.; Buzza, S.; Castleman, A. W. *J. Chem. Phys.* **1992**, *97*, 5243−5245.

(14) Castleman, A. W.; Guo, B. C.; Wei, S.; Chen, Z. Y. *Plasma Phys. Controlled Fusion* **1992**, *34*, 2047−2051.

(15) Pilgrim, J. S.; Duncan, M. A. *J. Am. Chem. Soc.* **1993**, *115*, 4395−4396.

(16) Castleman, A. W. *Z. Phys. D* **1993**, *D26*, 159−161.

(17) Wei, S.; Guo, B. C.; Purnell, J.; Buzza, S. A.; Castleman, A. W. *J. Phys. Chem.* **1993**, *97*, 9559−9561.

(18) Cartier, S. F.; May, B. D.; Castleman, A. W. *J. Chem. Phys.* **1994**, *100*, 5384−5386.

(19) Cartier, S. F.; May, B. D.; Castleman, A. W. *J. Am. Chem. Soc.* **1994**, *116*, 5295−5297.

(20) Byun, Y. G.; Lee, S. A.; Kan, S. Z.; Freiser, B. S.; Brown, H. C. *J. Phys. Chem.* **1996**, *100*, 14281−14288.

(21) Byun, Y. G.; Freiser, B. S. *J. Am. Chem. Soc.* **1996**, *118*, 3681−3686.

(22) Byun, Y. G.; Kan, S. Z.; Lee, S. A.; Kim, Y. H.; Miletic, M.; Bleil, R. E.; Kais, S.; Freiser, B. S. *J. Phys. Chem.* **1996**, *100*, 6336−6341.

(23) Chen, Z. Y.; Walder, G. J.; Castleman, A. W. *J. Phys. Chem.* **1992**, *96*, 9581−9582.

(24) Pilgrim, J. S.; Duncan, M. A. *J. Am. Chem. Soc.* **1993**, *115*, 9724−9727.

(25) Pilgrim, J. S.; Duncan, M. A. *J. Am. Chem. Soc.* **1993**, *115*, 6958−6961.

(26) Wei, S.; Guo, B. C.; Deng, H. T.; Kerns, K.; Purnell, J.; Buzza, S. A.; Castleman, A. W. *J. Am. Chem. Soc.* **1994**, *116*, 4475−4476.

(27) Cartier, S. F.; May, B. D.; Toleno, B. J.; Purnell, J.; Wei, S.; Castleman, A. W. *Chem. Phys. Lett.* **1994**, *220*, 23−28.

(28) Yeh, C. S.; Afzaal, S.; Lee, S. A.; Byun, G.; Freiser, B. S. *J. Am. Chem. Soc.* **1994**, *116*, 8806−8807.

(29) Purnell, J.; Wei, S.; Castleman, A. W. *Chem. Phys. Lett.* **1994**, *229*, 105−110.

(30) Pilgrim, J. S.; Brock, L. R.; Duncan, M. A. *J. Phys. Chem.* **1995**, *99*, 544−550.

(31) Pilgrim, J. S.; Duncan, M. A. *Int. J. Mass Spectrosc. Ion Processes* **1994**, *138*, 283−296.

(32) Pilgrim, J. S.; Duncan, M. A. *Adv. Met. Semicond. Clusters* **1995**, *3*, 181−221.

(33) Byun, Y. G.; Yeh, C. S.; Xu, Y. C.; Freiser, B. S. *J. Am. Chem. Soc.* **1995**, *117*, 8299−8303.

(34) Cartier, S. F.; May, B. D.; Castleman, A. W. *J. Chem. Phys.* **1996**, *104*, 3423−3432.

(35) Cartier, S. F.; May, B. D.; Castleman, A. W. *J. Phys. Chem.* **1996**, *100*, 8175−8179.

(36) Kan, S. Z.; Lee, S. A.; Freiser, B. S. *J. Mass Spectrom.* **1996**, *31*, 62−68.

(37) Chen, Z. Y.; Guo, B. C.; May, B. D.; Cartier, S. F.; Castleman, A. W. *Chem. Phys. Lett.* **1992**, *198*, 118−122.

(38) Brock, L. R.; Duncan, M. A. *J. Phys. Chem.* **1996**, *100*, 5654−5659.

(39) Wang, L. S.; Li, S.; Wu, H. *J. Phys. Chem.* **1996**, *100*, 19212−19214.

(40) Kerns, K. P.; Guo, B. C.; Deng, H. T.; Castleman, A. W. *J. Phys. Chem.* **1996**, *100*, 16817−16821.

(41) Chen, Z. Y.; Walder, G. J.; Castleman, A. W. *Phys. Rev. B* **1994**, *49*, 2739−2752.

(42) Li, S.; Wu, H.; Wang, L. S. *J. Am. Chem. Soc.* **1997**, *119*, 7417−7422.

(43) Deng, H. T.; Guo, B. C.; Kerns, K. P.; Castleman, A. W. *J. Phys. Chem.* **1994**, *98*, 13373−13378.

(44) Guo, B. C.; Wei, S.; Purnell, J.; Buzza, S.; Castleman, A. W. *Science* **1992**, *256*, 515−516.

(45) Guo, B. C.; Kerns, K. P.; Castleman, A. W. *J. Am. Chem. Soc.* **1993**, *115*, 7415−7418.

(46) Kerns, K. P.; Guo, B. C.; Deng, H. T.; Castleman, A. W. *J. Am. Chem. Soc.* **1995**, *117*, 4026−4029.

(47) Yeh, C. S.; Byun, Y. G.; Afzaal, S.; Kan, S. Z.; Lee, S.; Freiser, B. S.; Hay, P. J. *J. Am. Chem. Soc.* **1995**, *117*, 4042−4048.

(48) Byun, Y. G.; Lee, S. A.; Kan, S. Z.; Freiser, B. S.; Brown, H. C. *J. Phys. Chem.* **1996**, *100*, 14281−14288.

(49) Helden, G. v.; Gotts, N. G.; Maitre, P.; Bowers, M. T. *Chem. Phys. Lett.* **1994**, *227*, 601−608.

(50) Bowers, M. T. *Acc. Chem. Res.* **1994**, *27*, 324−332.

(51) Lee, S.; Gotts, N. G.; Helden, G. v.; Bowers, M. T. *Science* **1995**, *267*, 999−1001.

(52) Van Heijnsbergen, D.; von Helden, G.; Duncan, M. A.; van Roji, A. J. A.; Meijer, G. *Phys. Rev. Lett.* **1999**, *83*, 4983−4986.

(53) von Helden, G.; Tielens, A. G. G. M.; Van Heijnsbergen, D.; Duncan, M. A.; Hony, S.; Waters, L. B. F. M.; Meijer, G. *Science* **2000**, *88*, 313−316.

(54) Dance, I. G. *J. Chem. Soc., Chem. Commun.* **1992**, 1779−1780.

(55) Rohmer, M. M.; Benard, M.; Henriet, C.; Bo, C.; Poblet, J. M. *J. Chem. Soc., Chem. Commun.* **1993**, 1182−1185.

(56) Rohmer, M. M.; Benard, M.; Poblet, J. M. In *Metal Clusters in Chemistry*; Braunstein, P., Oro, L. A., Raithby, P. R., Eds.; VCH−Wiley: Weinheim, Germany, 1999; Vol. 3, pp 1664−1710.

(57) Rohmer, M. M.; Benard, M.; Poblet, J. M. *Chem. Rev.* **2000**, *100*, 495−542.

(58) Dance, I. G. *J. Am. Chem. Soc.* **1996**, *118*, 2699−2707.

(59) Cassady, C. J.; McElvany, S. W. *J. Am. Chem. Soc.* **1990**, *112*, 4788−4797.

(60) McElvany, S. W.; Cassady, C. J. *J. Phys. Chem.* **1990**, *94*, 2057−2062.

(61) Sosa, C.; Andzelm, J. W.; Elkin, B. C.; Wimmer, E.; Dobbs, K. D.; Dixon, D. A. *J. Phys. Chem.* **1992**, *96*, 6630−6636.

(62) Deeth, R. J. *Struct. Bonding* **1995**, *82*, 1−42.

(63) Guest, M. F.; Sherwood, P.; Fletcher, G. D.; Apra, E.; Nichols, J. A. In *ACS 212th Meeting, August 1996*; American Chemical Society: Washington, D.C., 1996; Abstract 367.

(64) Fan, L.; Ziegler, T. In *Density Functional Theory of Molecules, Clusters and Solids*; Ellis, D. E., Ed.; Kluwer: Dordrecht, The Netherlands, 1995; pp 67−95.

(65) Frankcombe, K. E.; Cavell, K. J.; Yates, B. F.; Knott, R. B. *J. Phys. Chem.* **1996**, *100*, 18363−18370.

(66) Jacobsen, H.; Berke, H. *Chem. Eur. J.* **1997**, *3*, 881−886.

(67) Scheiner, A. C.; Baker, J.; Andzelm, J. W. *J. Comput. Chem.* **1997**, *18*, 775−795.

(68) Curtiss, L. A.; Raghavachari, K.; Redfern, P. C.; Pople, J. A. *J. Chem. Phys.* **1997**, *106*, 1063−1079.

(69) Bruyndonckx, R.; Daul, C.; Manoharan, P. T.; Deiss, E. *Inorg. Chem.* **1997**, *36*, 4251−4256.

(70) Seminario, J. M.; Politzer, P. *Modern Density Functional Theory. A Tool for Chemistry*; Elsevier: Amsterdam, 1995; Vol. 2.

(71) Delley, B. In *Modern Density Functional Theory: A Tool for Chemistry*; Seminario, J. M., Politzer, P., Eds.; Elsevier: Amsterdam, 1995; Vol. 2, pp 221−254.

(72) Hutter, J.; Lüthi, H. P.; Diederich, F. *J. Am. Chem. Soc.* **1994**, *116*, 750−756.

(73) Delley, B.; Wrinn, M.; Lüthi, H. P. *J. Chem. Phys.* **1994**, *100*, 5785−5791.

(74) Smith, B. J.; Radom, L. *Chem. Phys. Lett.* **1994**, *231*, 345−351.

(75) Dance, I. G.; Fisher, K. J. *J. Chem. Soc., Dalton Trans.* **1997**, 2563−2575.

(76) Dance, I. *J. Chem. Soc., Chem. Commun.* **1998**, 523−530.

(77) Delley, B. *New J. Chem.* **1992**, *16*, 1103−1107.

(78) Delley, B. *J. Chem. Phys.* **1990**, *92*, 508−517.

(79) Lee, C.; Yang, W.; Parr, R. G. *Phys. Rev. B* **1988**, *37*, 785−789.

(80) Becke, A. D. *Phys. Rev. A* **1988**, *38*, 3098.

(81) Dance, I. G. *J. Am. Chem. Soc.* **1996**, *118*, 6309−6310.

(82) Chen, H.; Feyereisen, M.; Long, X. P.; Fitzgerald, G. *Phys. Rev. Lett.* **1993**, *71*, 1732−1735.

(83) Pauling, L. *Proc. Natl. Acad. Sci. U.S.A.* **1992**, *89*, 8175−8176.

(84) Khan, A. *J. Phys. Chem.* **1993**, *97*, 10937−10941.

(85) Ceulemans, A.; Fowler, P. W. *J. Chem. Soc., Faraday Trans. 1* **1992**, *88*, 2797−2798.

(86) Lou, L.; Nordlander, P. *Chem. Phys. Lett.* **1994**, *224*, 439−444.